

 M 2019

U. PORTO
FEUP FACULDADE DE ENGENHARIA
UNIVERSIDADE DO PORTO

DESIGN OF A THERMOGRAPHIC SETUP AND APPLICATIONS TO PEM FUEL CELLS

ANA SÍLVIA OLIVEIRA DA SILVA

MASTER THESIS PRESENTED TO THE FACULTY OF ENGINEERING OF THE UNIVERSITY OF PORTO

CHEMICAL ENGINEERING

Master in Chemical Engineering

Design of a Thermographic Setup and Applications to PEM Fuel Cells

A Master's dissertation

by

Ana Sílvia Oliveira da Silva

Developed within the course of Dissertation

Held in

German Aerospace Center



Supervisor at FEUP: Prof. Adélio Mendes

Supervisor at DLR: Indro Biswas

Chemical Engineering Department



December of 2019

© Ana Sílvia Oliveira da Silva

ACKNOWLEDGEMENTS

I would like to express my deepest gratitude to my supervisors, Indro and Adélio, for all their time, support, constant guidance and friendship, they were my truly support during the hardest times. To Indro, I apologize for all the times I asked you dumb questions and you always replied with a smile and patience. Thank you for always giving me the freedom to explore and your sapient words. I will miss our long conversations on random topics; I truly believe to have discover a very good heart in you. To professor Adélio, I want to express my personal gratitude for the times you motivated me in Portugal to enter this journey, for the long phone calls where you shared with me an infinitesimal percentage of your wisdom, for being so kind and straight! Thank you both. A special appreciation to Tiago Lagarteira who helped me before everything even start.

Many others contributed both to this work and for one of the best times I experienced in life. A special thanks to the electrochemistry group: Torsten Knori, Mathias Schulze, Peter Mahnke, Daniel Garcia, Krishan, Pia and Siggy for all the guidance and expertise that highly contributed to the successful achievement of this work at DLR. To my friends for life Daniel, Ambu and Abi, I just have no words to describe how much I love you, how much my life in Germany was incredibly fascinating, immensely due to your friendship. The times I cried both for happiness and struggle, you've always been there.

Finally, on a personal note, to my parents. I am inexpressibly blessed for being your daughter. My infinite gratitude for all your support, motivation, believing and unconditional love along this long path. I owe you everything!

To my person, Miguel. Thank you for enlightening me and show me the way. We know the meaning of your support and your persistence to me. You are my rock! You are my model of dedication, determination, persistence, ambition and heart. Thank you for your love and support and for believing in my potential, specially at those moments when I did not.

Overall, this thesis has been a fascinating journey. I would do it again, I confess with a lot of changes, but I am grateful how it changed my life and showed me what I want for the closest future. This work made me a better student, a better professional, and I hope the foremost, a better person. Thank you!

Ana Sílvia Oliveira da Silva

Plieningen, Stuttgart, December 2019

ABSTRACT

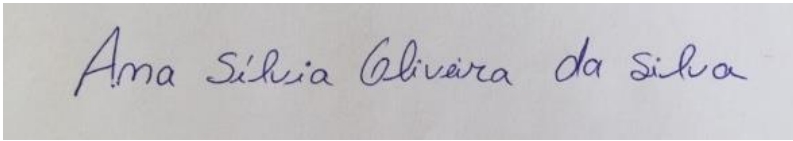
Proton exchange membrane fuel cells are one of the most promising technologies for achieving a clean energy source. One of the hardest barriers to overcome is the fact that it is still not a viable market option, due to the excessive costs of Platine, the catalyst. Another aspect that has been constantly developed is its performance, in order to achieve a more competitive industry. Studies on performance are closely related with studies on water and heat management within the fuel cell. With this work, we are one step forward to understand this complex heat and water phenomena that many groups around the world have been trying to understand and that strongly limits the achievement of a better performance.

With this novel and ex-situ technique, many complex physical and chemical processes can be developed. With thermography, water management is some steps closer to be fully understood and its compromise to achieve a better performance and long-life. Thermography revealed to be a powerful technique to analyze cathode water accumulation, both formation and drying. The solid-liquid interactions in the channels can be further studied, as well as local temperature distributions.

Key-words: PEMFC, fuel cell, thermography, water transport, GDL, water management, flooding, drying, lens, infrared.

Declaration

I hereby declare, on my word of honour, that this work is original and that all non-original contributions were properly referenced with source identification.



Ama Sílvia Oliveira da Silva

Table of Contents

ACKNOWLEDGEMENTS	i
ABSTRACT	iii
Declaration	v
NOTATION AND GLOSSARY.....	ix
1 Introduction	1
1.1 Framework and description of the project.....	1
1.2 Presentation of the Institution	3
1.3 Contributions of the work.....	4
1.4 Structure of the thesis	4
2 State of the art	6
2.1 PEM fuel cells.....	6
2.1.1 Thermodynamics of the PEMFC	8
2.1.2 Components & Cell Assembly.....	10
2.1.3 Water Management.....	15
2.2 Fuel Cell Monitoring.....	16
2.3 Thermography.....	18
2.3.1 Infrared radiation.....	18
2.3.2 Infrared Cameras.....	20
3 Setup	22
3.1 Fuel Cell & Test Bench.....	22
3.2 IR camera before being adapted.....	26
3.3 Materials used for (further) development	27
3.3.1 Lenses & other elements	27
Iris diaphragms:	29
3.3.2 Infrared Transparent Window	30
4 Results: Applications & limitations	32
4.1 Modifications and Improvement of the FC.....	32
4.2 Thermography	33
4.2.1 Intrinsic magnification/full view.....	33
4.2.2 Magnifying Setup.....	34
4.2.3 Iris Aperture effect.....	40
4.2.4 Indexing the ribs.....	41
4.2.5 Applications and Limits.....	42

5	Conclusions.....	44
5.1	Accomplished objectives	44
5.2	Limitations (Out look) and Future Work.....	44
5.3	Final appreciation.....	45
6	References.....	47
7	Appendix	50

NOTATION AND GLOSSARY

List of Acronyms

AR	Anti-reflective
CCM	Catalyst coated membrane
FC	Fuel Cell
FCC	Face centered cubic
GDL	Gas diffusion layer
HOR	Hydrogen oxidation reaction
IR	Infrared
MEA	Membrane electrode assembly
OCV	Open circuit voltage
ORR	Oxygen reduction reaction
PCB	Printed circuit board
PEM	Proton exchange membrane

Greek letters

σ	Stephan-Boltzmann constant	$5.670 \cdot 10^{-8} \text{ W} \cdot \text{m}^{-2} \cdot \text{K}^{-4}$
----------	----------------------------	---

Latin letters

A	Area	m^2
B_λ	Spectral radiance of a blackbody	$\text{W} \cdot \text{m}^{-3}$
c	Speed of light	$\text{m} \cdot \text{s}^{-1}$
d_o	Lens-to-object distance	m
d_i	Lens-to-image distance	m
E	Electrode potential	V
e	emissivity	$\text{W} \cdot \text{m}^{-2} \cdot \mu\text{m}^{-1}$
F	Faraday constant	$96485 \text{ C} \cdot \text{mol}^{-1}$
f	focal length	
G	Gibbs free energy	J
h	Planck constant	$\text{J} \cdot \text{s}$
H	Enthalpy	J
h_i	Image height	m
h_o	Object height	m
i	Current density	$\text{A} \cdot \text{m}^{-2}$
I	Current	A
j	Energy flow density	$\text{J} \cdot \text{m}^{-2} \cdot \text{s}^{-1}$

K_B	Boltzmann constant	$J \cdot K^{-1}$
M	Magnification	-
$n(\lambda)$	refractive index	-
	number of moles of electrons	
n	transferred	mol
P	Thermal energy radiated per second	$J \cdot s^{-1}$
P	Pressure	bar
R^*	Universal gas constant	$J \cdot mol^{-1} \cdot K^{-1}$
R	Resistance	Ω
T	Temperature	K

1 Introduction

1.1 Framework and description of the project

Providing a clean, safe and reliable energy supply around the world is the basic driver for a sustainable high quality of life. For human activities to co-exist with a sustainable environment, energy supply systems must provide both societal needs at affordable prices and not impact negatively the planet. Those systems need to relieve the effects of climate change, reduce toxic pollutants and be in place to replace the diminishing reserves of oil, in order to provide a sustainable equilibrium on the economy and on public health [1]. Sørensen in 1975 was the first to suggest that all energy needs in society could derive from renewable resources [2]. So, there is a common acceptance that current hydrocarbon fuels need to be substituted by low-carbon alternatives if global greenhouse gas emissions are to be drastically reduced until 2050 to prevent dangerous climate changes [3]. The global demand for every primary energy source increases between 2012 and 2040, but the rates of growth are considerably different as seen in **table 1** [4].

Table 1: World primary energy demand by fuel [4]

	1990	2012	2020	2025	2030	2035	2040	CAAGR* 2012-2040
Coal	2 231	3 879	4 211	4 293	4 342	4 392	4 448	0.5%
Oil	3 232	4 194	4 487	4 612	4 689	4 730	4 761	0.5%
Gas	1 668	2 844	3 182	3 487	3 797	4 112	4 418	1.6%
Nuclear	526	642	845	937	1 047	1 137	1 210	2.3%
Hydro	184	316	392	430	469	503	535	1.9%
Bioenergy**	905	1 344	1 554	1 675	1 796	1 911	2 002	1.4%
Other renewables	36	142	308	435	581	744	918	6.9%
Total	8 782	13 361	14 978	15 871	16 720	17 529	18 293	1.1%

*Compound average annual growth rate. ** Includes traditional and modern uses of biomass.

The share of fossil fuels has remained broadly constant over the past three decades but falls gradually until 2040; despite these fuels are still dominant in 2040, we can see on **figure 1** that renewable energy sources are growing faster than any other fuel [4].

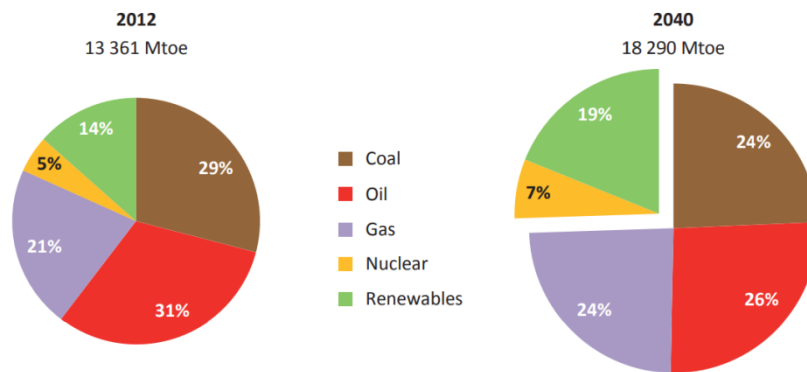


Figure 1: Fuel shares in the world primary energy demand [4]

Hydrogen energy systems seems to be one of the most effective solutions and play a significant role in providing a better environment and sustainability [5]. Kwak et al. [6] affirm that the new hydrogen powered fuel cells are more efficient and cleaner than conventional energy technologies and can be the base of a future sustainable energy system. The first approach to a fuel cell was developed by Sir William Groove in England in the 1800s, with the first sketch published in 1843. The actual utilization of the concept came in 1960 when NASA started developing research for methods for generating power for space vehicles [1]. As shown in table 1, there is an increase demand for energy conversion energies. Mankind needs a solution that runs on alternative fuels, has higher efficiency than the internal combustion engines, operate independently of the weather and mitigate the environmental impact. Fuel cells incorporate these attributes, this makes them to be considered a prominent power source for the 21st century.

The PEMFC - the proton exchange membrane fuel cells - has received great amount of research and development in the last years. It operates at low temperatures, has a quick start-up and is comparatively simple in their construction. Nevertheless, to become economically viable, some barriers as cost, hydrogen storage, lifetime and reliability need to be overcome. The operation of a PEM fuel cell is deeply connected to the presence of water in the cell, thus, the water management is critical and one of the most widely studied topics in PEMFC technology. An adequate water management requires an optimum balance between two opposite needs: good membrane hydration and dry gas diffusion media to prevent gas blockage by water flooding within the cell [7]. Therefore, there is a necessity of developing a technology to study water transport, particularly to predict the high levels of saturation of the liquid water in the flow channels [8].

Different techniques to analyze temperature and water management in situ were used, such as segmented cell, micro-thermocouples, neutron radiography but many phenomena are still

far from being understood, remaining a lack of models to describe this phenomena and other models to be validated.

Thermography is an imaging technology that allows to monitor the thermal radiance that a surface emits. This technology is used outside the system under analysis and for this is a non-contact and non-interfering technology to analyze systems, bringing an advantage when compared with the previous mentioned.

The purpose of this innovative work is to develop a new cell design and an adequate optical system to “look” directly into the cell to study both heat and water management. Understand how these mechanisms are correlated and influence the performance of the fuel cells leads us to achieve a better performance and thus, economically more viable cells.

1.2 Presentation of the Institution

DLR - Deutsches Zentrum für Luft-und Raumfahrt - is a research center of the Federal Republic of Germany whose research is centered in aviation, space, energy, transport, security and digitalization. The oldest predecessor organization of DLR was found in 1907 in Göttingen and in 1997 the name became the one we know nowadays. DLR is present in 20 locations in Germany and has 4 international offices: Brussels, Paris, Tokyo and Washington D.C., with about 8.000 employees.

In Stuttgart, DLR is situated in Pfaffenwaldring 38-40 with about 700 employees. The main research areas include high performance structures made from ceramic fiber, polymer and hybrid composites, innovative road and rail vehicle concepts, laser system development, energy storage and conversion technologies, gas turbines and combustion processes and the development of receivers for solar power plants. The DLR site in Stuttgart has its origin in the Research Institute of Jet Propulsion Physics, established in 1954 at Stuttgart airport. As a result of its geographic proximity to the neighboring University of Stuttgart, together with the close collaboration in research and education, the DLR site has become an important part of the scientific community in Stuttgart. DLR Stuttgart has 6 institutes: Institute of Structures and Design, Institute of Vehicle Concepts, Institute of Technical Physics, Institute of Combustion Technology, Institute of Solar Research and Institute of Engineering Thermodynamics. The present work was developed in the Institute of Engineering Thermodynamics. This institute counts with 180 scientific and technical employees, engineers and doctoral candidates. DLR Stuttgart actively supports the training of young scientists and engineers, through teams, joint projects and the participation of DLR scientists in the

learning process by receiving students from the University to have the experience of developing their bachelor or master thesis in its institutes.

The spectrum of activities ranges from theoretical studies to laboratory work for basic research and to the operation of pilot plants. These experimental and theoretical studies are accompanied by systems analysis studies to analyze the associated technological, environmental and economic potential and situate it in a larger overall context of the energy economy by means of scenarios [9]. Within this Institute, the present work was developed in the Department of Electrochemical Energy Technology, headed by Prof. K. Andreas Friedrich, with a team of 60 people on the development of efficient electrochemical energy converters, primarily batteries, fuel cells and electrolyzers. Activities range from cell design, manufacturing and diagnostics to system optimization and demonstration. The main challenges of electrochemical energy technology are to find solutions to overcome the trade-offs between efficiency, operating time, comfort, safety and cost.

1.3 Contributions of the work

This work is contributing for the study of some phenomena within the cell that are nowadays not completely understood and that contribute for the performance of the cell. With the thermographic technique and since it is a technique that does not interfere in the system, it is possible to observe that water management can be tracked, and a map of water and heat distributions can be achieved. This lead us one step closer to create improved fuel cells, by explaining the interaction of mechanisms, leading fuel cells to be a viable market option as a clean sustainable energy source. The work is a first approach to thermography, thus, there is lot of work to be developed. Yet, this work showed successfully that this technique has a great potential both for magnified and non-magnified setups, despite some actual limitations that need to be corrected and improved.

1.4 Structure of the thesis

This thesis is composed by five main chapters: Introduction, State of the Art, Materials, Results (including applications and limitations) and by last the Conclusions.

In the first chapter, Introduction, it is presented the context of the work, the institution where it was developed and the contribution of this work for the field of fuel cells.

In the chapter two, State of the Art, the author describes the fuel cell technology and challenges based on the literature and introduces the theory for thermographic viewing, through physical explanation of the technology.

In the third chapter, Materials, the author describes the test-bench and the fuel cell used for this work, presents the infrared camera as it comes from the brand and introduces the materials used to develop the optical system of analyses, such as lenses and other optical elements. All the software used are also presented in this chapter.

The Results include the applications and limitations of this technique, it's where the work done is fully explained as well its applications and limitations that need to be improved.

To complete this work, the conclusions and following work are exposed in the fifth chapter.

2 State of the art

The electrochemical conversion of energy is the conversion of chemical energy to electrical energy or vice versa. A fuel cell is an electrochemical device that converts free energy of a chemical reaction into electrical energy continuously as long as the fuel, hydrogen and oxidant are supplied.

The conversion of hydrogen to energy can be achieved through many means including internal combustion engines and batteries but the most efficient method is to use a fuel cell where the chemical energy of hydrogen is directly converted into electrical energy and the only by-products are water and heat, which potentially have less environmental impact than internal combustion engines. For this reason, fuel cells are considered as prominent power sources for the future. The applications of fuel cells can be divided in three categories: portable power generation, stationary power generation and transportation [10].

It is clear that from one kind of cell to another the reactions vary, and thus, so do the types of fuel. There are 6 major categories of fuel cells named according to the electrolyte used in it. The type of electrolyte determines the kind of chemical reaction, the kind of catalyst needed, the temperature range, and the type of fuel. All these characteristics affect the applications the cells are most suitable for. It's possible to group these types in 2 groups according to the temperature range of operation: the high temperature and the low temperature fuel cells - HTFC and LTFC- respectively. The low-to-medium temperature fuel cells are limited by the requirement of noble metal electrocatalysts for optimum reaction rates at the anode and cathode, and H₂ is the most recommended fuel. For high-temperature fuel cells the catalyst restrictions are less stringent, and the fuel types can vary [11]. Among the various types of fuel cells, the PEMFC operating at low temperature are currently leading the commercial front for its advantages such as high power density, low temperature operation, quick start-up time, rapid response to varying loads and dynamic operation capabilities [12], [13].

2.1 PEM fuel cells

The proton exchange membrane fuel cells -PEMFC- belong to the family of low temperatures fuel cells (below 100 °C), generate a specific power ($W \cdot kg^{-1}$) and its power density ($g \cdot W^{-1}$) is higher than any other type of fuel cell [12]. For these reasons, PEMFC are expected to be an interesting alternative as power supply, but still some barriers have to overcome before PEMFC become actually a viable market option, as discussed below [14].

The three key components of PEM fuel cells are: membrane-electrode assembly (MEA), sealing gaskets and bipolar plates.

MEA is the heart of the fuel cell, consisting in a membrane (electrolyte), 2 catalyst layers (anode and cathode) and 2 gas diffusion layers (GDL). As shown in **figure 2**, the membrane is sandwiched between the electrodes. A MEA with this configuration is known as a 5-layer MEA.

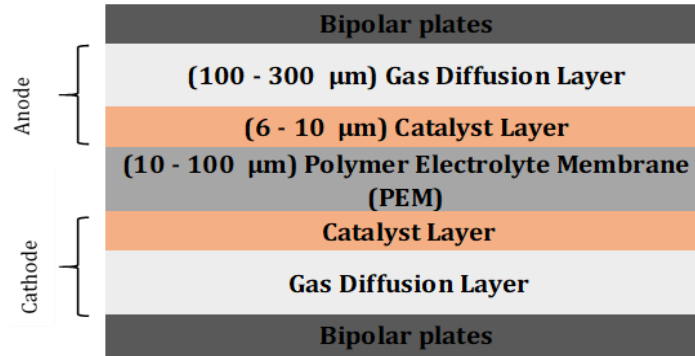


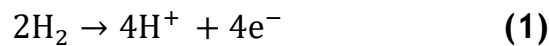
Figure 2: Basic scheme of a PEMFC

The 5-layer commercial MEA is ready to be installed in a cell as an integrated component.

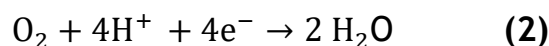
During the fuel cell operation, two electrochemical half-cell reactions take place in the surface of both catalysts, in parallel: one in the anode side, the other at the cathode side.

See **figure 3** for a better understanding of the following explanation.

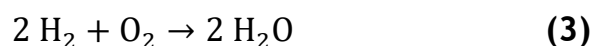
The **anode** electrode is continuously fed with the fuel gas hydrogen, which flows through the GDL to the catalyst anode. In the surface of the catalyst anode, hydrogen is spontaneously oxidized into hydrogen ions and electrons, due to the presence of the Platinum catalyst, a reaction named hydrogen oxidation reaction, HOR, see **equation (1)**.



These hydrogen protons H^+ pass through the membrane (electrolyte) to the **cathode** electrode where oxygen (or air) is being fed continuously. The electrons pass through an external circuit and reach the cathode. In the cathode, oxygen is combined with hydrogen protons and electrons catalytically to form water, a reaction named oxygen reduction reaction, ORR, see **equation (2)**.



The overall reaction is then:



This overall **reaction (3)** is spontaneous and exothermic, and the by-product water leaves the

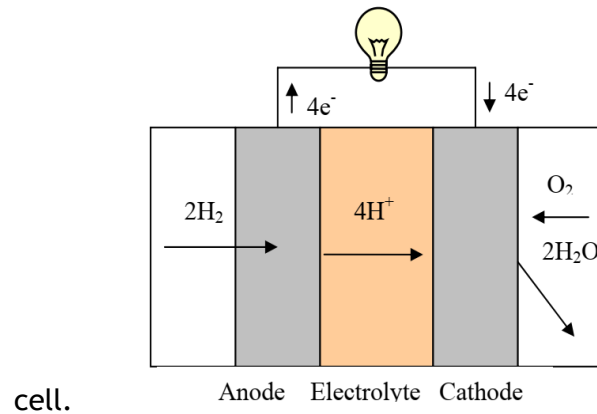


Figure 3: Scheme of an operating fuel cell [27]

2.1.1 Thermodynamics of the PEMFC

From a thermodynamically point of view, the maximum work output obtained from the **equation (3)** is related with the change in the Gibbs free energy, ΔG (energy available to do external work, neglecting any work done by changes in the pressure and/or volume) of the reaction. In a fuel cell, the external work involves the movement of electrons around the external circuit. We evaluate ΔG with the difference in the free energy of the products minus that of the reactants. This reaction is thermodynamically favoured because the free energy of the products is less than that of the reactants. The standard free energy change of the fuel cell reaction is indicated by the **equation (4)**, when the reactants and products are in their standard states

$$\Delta G^0 = -nFE^0 \quad (4)$$

where ΔG^0 the free energy change, n is the number of moles of electrons involved, E is the reversible potential and F the Faraday constant.

The theoretical equilibrium potential (E^0) for H_2/O_2 fuel cell is 1.229 V at 25 °C and 1 atm pressure [15].

The thermodynamic equilibrium potential at operating temperature and pressure different from 25 °C and 1 atm can be calculated from the Nernst **equation (5)**:

$$E = E^0 + \frac{RT}{2F} \ln \left(\frac{P_{H_2} \times P_{O_2}^{0.5}}{P_{H_2O}} \right) \quad (5)$$

where P are the partial pressures of reactants and products (atm), T is the temperature (K), R is the gases constant ($J \cdot kg^{-1} \cdot K^{-1}$) and F Faraday's constant ($C \cdot g^{-1} \cdot mole$) [11], [15]. According to this equation, the ideal cell potential at a given temperature can be increased by operating the cell at higher reactant pressures. The ideal and actual performance of a fuel cell is quite

low than the theoretical value of 1.229 V when we analyze the potential current response of the cell, as explained below.

Chemical energy is converted in electrical energy when a current is drawn, but the actual cell potential is lowered from its equilibrium potential due to irreversible energy losses, called polarization losses or overpotential. There are several factors which contribute to these losses, such as pressure of the reactant gases, relative humidity of the reactants, fuel cell temperature, flowfield design, MEA characteristics among others.

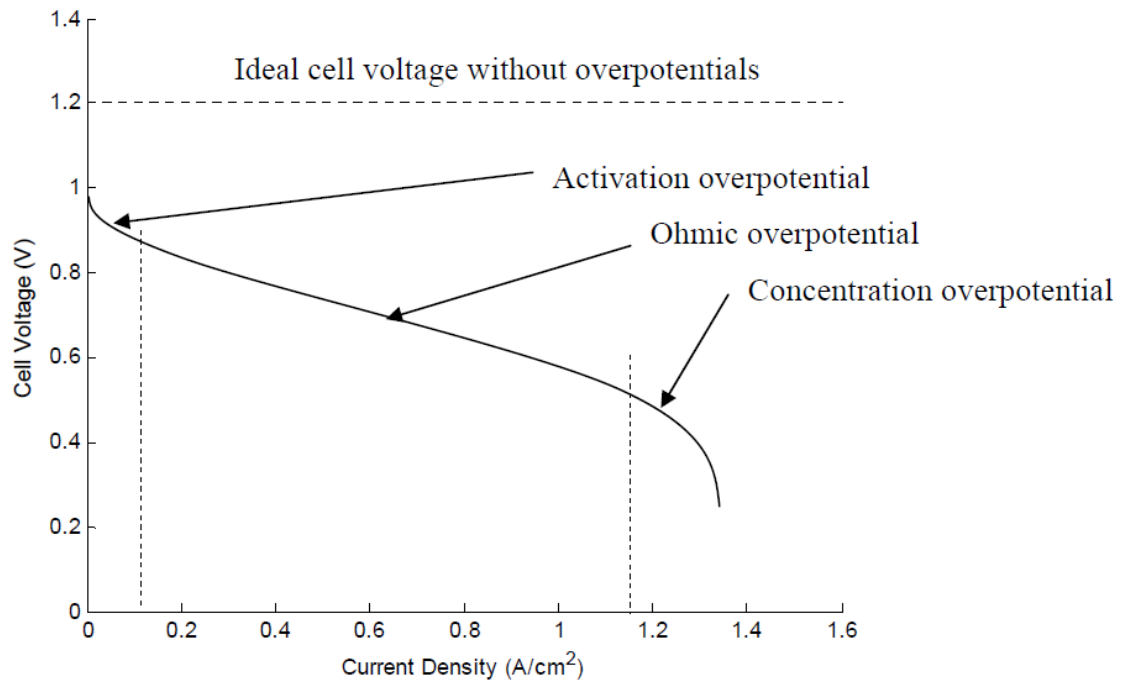


Figure 4: Typical polarization curve of a PEM fuel cell [11]

Fuel cell performance is directly influenced by various thermodynamic, electrochemical and operating variables, such as membrane material and thickness, platinum loading, flowfield design, cell temperature, cell pressure, gas concentration, current density, relative humidity of reactants, etc.

To maintain high efficiency, a fuel cell usually works in the ohmic overpotential region. Here, the membrane resistance is the major resistance and varies with water content in the membrane. The flow rate and the relative humidity of the reactants affect the humidity of the membrane. Dry membrane results in low membrane conductivity; on the other hand, too much water in the fuel cell causes flooding and high losses of potential.

Thus, a critical issue that has severely limited the application of PEMFC, influencing both performance and life under transient loading is the water accumulation and distribution in the cell. Water accumulation also influences the warm-up or shut down procedure for PEMFC that need to work under freezing temperature. There are currently four areas of research in

PEMFC: modelling of fuel cell performance, flowfield design, dynamic fuel cell models and experiments about water transport.

Overall, it is honest to declare that in parallel to the costs, water management is one of the most important remaining points for the adoption of PEMFC.

2.1.2 Components & Cell Assembly

As previously mentioned, the key components of a PEMFC are:

- I. membrane-electrode assembly (MEA)
- II. two bipolar plates and flowfield

Manufacturers such as DuPont/Dow Chemical, Gore, SGL, 3M and Johnson Matthey are positioning themselves to become world suppliers of PEMFC components [12]. The commercialization of PEMFC is struggled by two main aspects: durability of some key components like membranes and electrodes and the high cost of the systems. The durability of a PEM fuel cell depends mainly on the membrane-electrode assembly (MEA), while the high costs critically depend on the Pt content on the catalyst layer. Platinum costs a large parcel on the total cost due to its high price and limited supply. Catalyst costs 55% of the total cost, while the membrane costs 7%, 10% of the cost belong to the bipolar plates and 10% to the gas diffusion layers. Developing high-performance, cost-effective and durable electrocatalysts is the first priority for PEMFC development [12].

I. Membrane-Electrode Assembly (MEA)

MEA is called the “heart of the fuel cell” because it is crucial to the success of this technology. The MEA consists of:

- proton conducting membrane (PCM)
- two catalyst layers (anode and cathode)
- two gas diffusion layers (GDL)

MEA assembly primary focus is to achieve good contact between the membrane, the GDL and the catalyst layers. The membrane is the core of the fuel cell, separating the reduction and oxidation half-reactions. It allows the protons H^+ to pass through it to complete the overall reaction, and prevents the electrons e^- to pass, forcing them to go through an external circuit, generating the usable electric current. The catalyst layers promote each half-reaction. The gas diffusion layers improve the efficiency of the cell by allowing direct access of the reactants to the catalyst layers while stimulating the removal of excess water.

The **proton conducting membrane (PCM)** is desired to have good chemical, mechanical and electrochemical stability, high proton conductivity and zero electric conductivity, thermal and hydrolytic stability, chemical properties compatible with the electrodes, no permeable to reactants, high durability and low cost [12]. Rao et al. stated that the most used membrane material is perfluorosulfonic acid (PFSA, or DuPont's Nafion®) [16]. This is due to its high proton conductivity and moderate growth in water. Nafion® combines three functional regions: (1) backbone: hydrophobic structure made of polytetrafluoroethylene (PTFE, DuPont's Teflon™); (2) hydrophilic side chains of $-O-CF_2-CF-O-CF_2-CF_2-$ which connect PTFE to the (3) ion clusters, which consists of sulfonic acid ions SO_3^- , that attracts H^+ [12]. When the membrane becomes hydrated, the hydrogen ions in the third region are bonded to the water molecules, becoming movable between sulfonic acid sites, see figure 5 [17].

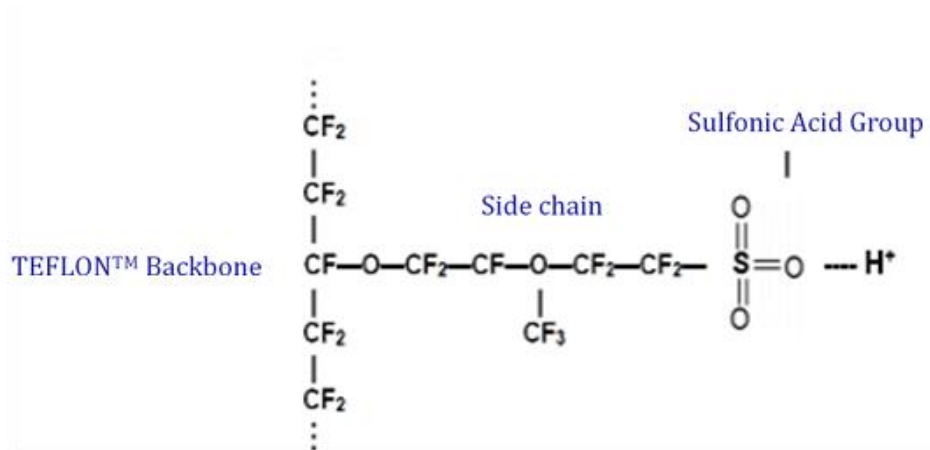


Figure 5: Chemical structure of Nafion or PFSA[17]

The advantages of using PFSA are first due to its backbone structure, which makes the membrane relatively strong and stable both for oxidative and reductive environments and second, the protonic conductivity achieved in a high humidified PFSA membrane can reach $0.2 \text{ S}\cdot\text{cm}^{-1}$, which means a cell resistance as low as $0.05 \text{ }\Omega \text{ cm}^2$ for a $100 \text{ }\mu\text{m}$ thickness with voltage loss of only 50 mV at $1 \text{ A}\cdot\text{cm}^{-2}$ [12], [13]. The proton conductivity in Nafion is related with its water content. At high and low humidity, the mechanism of proton transport varies, as discussed further. On the other hand, the disadvantages of PFSA membranes are related not only to its high cost but also to issues as safety, equipment requirements and temperature limitations. First, concerning the safety, above $150 \text{ }^\circ\text{C}$, toxic and corrosive gases are liberated [13]. Second, the equipment requirements to humidify the membrane will add high complexity and cost to the applications, for example in vehicle powertrain. By last, at high temperatures PFSA membrane properties degrade. As an example, the conductivity at $80 \text{ }^\circ\text{C}$ is diminished by more than 10 times in comparison to that at $60 \text{ }^\circ\text{C}$ [13].

The **Electrode catalyst layers - anode and cathode** - is where the two half-reactions, hydrogen oxidation reaction (HOR) and oxygen reduction reaction (ORR) take place. The catalyst layers in a PEM fuel cell consist in a film catalyst bonded to the membrane, one at the anode side, one at the cathode side. This catalyst is usually carbon-supported in a porous microstructure due to its large surface area, high electrical conductivity and well-developed pore structure. Usually, Platinum is considered as the best catalyst for these reactions, the so-called Pt/C catalysts. Platinum is therefore supported in carbon to avoid its agglomeration and to reduce the catalyst loading; yet, the high cost of Pt is motivating the search for alternatives. On the anode side, the HOR occurs with a faster kinetics than the ORR in the cathode, besides, reactions in the anode side are more complex, what demand a stable catalyst under extremely corrosive conditions, but still capable of activate O₂, that's why the catalyst loading is usually higher in the cathode than in the anode [18]. The electrode must be, both electrons and protons conductive to drive, respectively, electrons to the external current circuit and the migration of the protons through the membrane [19]. The cathode is responsible for about one third of the performance losses, due to the limitations of the ORR catalyst. The ORR is a challenging reaction to catalyse because the catalyst needs to be: (i) stable under extremely corrosive environments, (ii) chemically active to be able to activate O₂ and (iii) noble enough to release oxygen from the surface in H₂O form. Although platinum is the most promising catalyst for ORR due its good activity and stability, it is very expensive and there is a huge focus to reduce the Pt loading or to find alternative non-noble metal catalysts. Efforts are being made to reduce this Pt loading by: (i) increase the Pt catalytic activity by incorporating transition metals and (ii) improving its utilization by increase the surface area and its dispersion using high surface area supports.

The Gas diffusion layer (GDL): The two GDL are directly adjacent to the bipolar plates, one in the anode and another in the cathode side; their function is crucial to promote diffusion of reactants into the catalysts; each gas diffusion layer typically consist of two layers: the macroporous and the microporous layers, with a total thickness between 100-300 µm. The macroporous layers are in contact with the flowfields and the microporous layers are in contact with the electrode. The macroporous layer consists of a carbon fibre matrix with a large void volume, ~75 - 85% and microporous layers consist of porous carbon black mixed with fluoropolymer and are provided with a hydrophobic PFTE (Teflon) coating to ensure that his porous don't become congested with liquid water [20]. The main functions of GDL are assure that gas reactants effectively diffuse to the catalyst layer, minimize mass transport overpotential, assist in the water management, allowing water vapor to diffuse across the

MEA and providing a network of paths for liquid water to move from the MEA to the flow channel to prevent flooding and transport of the electrons for the external circuit [12], [21], [22]. In sum, “an optimum GDL is one that allows an appropriate amount of water vapour to reach the membrane/electrode interface, keeping the membrane humidified and thereby improving the cell efficiency. It allows the liquid water produced at the cathode to leave the cell and avoids flooding [12].” Some of the most common commercial GDLs for PEM fuel cells are Sigracet®, Ballard, Toray, Freudenberg, E-TEK and Tenax.

II. Bipolar plates and flowfield

The two bipolar plates are placed on the extremities of the cell, occupying the major volume and weight of the fuel cell and they embody the flowfields. Their functions are separate individual cells in a stack, conduct electrons, supply and uniformly distribute reactants over the flow channels and drive out generated liquid water and for that they need to be rigid and electrically conductive structures. The power density generated and water management at a fuel cell can be highly influenced by the flowfield design on the bipolar plates [23]. Thus, the flowfield design is an important factor in designing a PEMFC, as previous referred on section 2.1.1. The flowfield is thought to provide an adequate amount of the reactants to the GDL. The most popular channel configurations are single and multi-serpentines, parallel and interdigitated, see **figure 6**. As described later, can occur water flooding in the anode, so, serpentine arrangement is the most used for small PEM fuel cells.

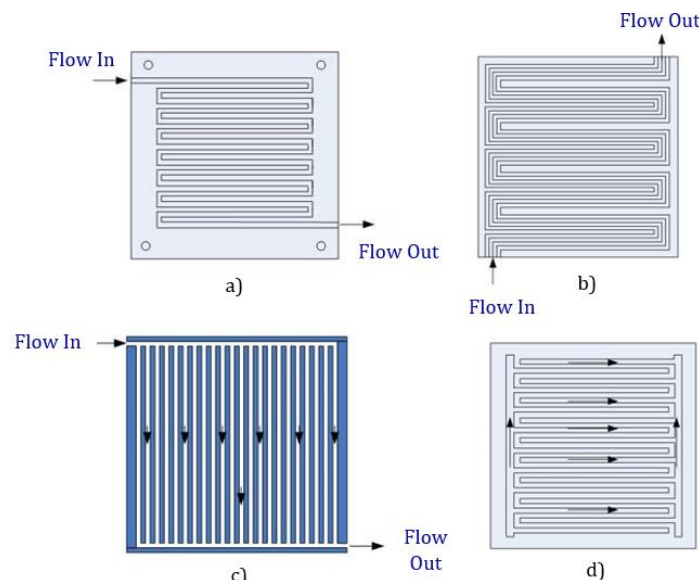


Figure 6: (a) and (b) single and multiple serpentine flowfield; (c) and (d) parallel and interdigitated flowfield

The single serpentine flowfield a) has a continuous linear channel from the inlet to the outlet; they are arranged parallel to one another but skewed to the edge of the plate. It is relatively

efficient at providing flow distribution across the electrode surface. It may cause pressure drop due to the long flow path. An advantage of this design is that accumulated water droplets are automatically driven out of the cell by the pressure. The disadvantage is that the reactant is depleted through the length of the channel, that is why with this design, an accurate amount of reactants must be provided. Some problems may arise due to the cathode flow and water management. When the cell operates for long periods, there is water accumulation in the cathode and its necessary pressure to move water out of the channels.

The multiple-serpentine flowfield b) is similar to the previous but there are several flow channels in continuous to limit the pressure drop. It prevents “dead areas” in the cathode surface due to water accumulation. The pressure drop here is lower than in the single serpentine but is still high due to the long flow path of each channel.

The parallel flowfield c) requires less mass flow per channel and provides more uniform gas distribution and a lower pressure drop. When oxidant is oxygen, it can occur low and unstable cell voltages after long periods of operation due to water buildup in the channels. The disadvantage in this configuration is that an obstruction in one channel results in unequal gas redistribution among the other channels and a dead zone downstream the obstruction.

The interdigitated flowfield d) consists of multiple dead - ended flow channels. Its principle is based on the fact that gas is forced to flow through the adjacent GDL and then to the electrode when the reaction occurs, while the excess reactant gases return through GDL to the flowfield channel to the outlet. It's not very common in PEMFC.

Cell Assembly

It is crucial to assembly all the previous mentioned components precisely positioned, although in laboratories, PEM fuel cells are manually assembled. Therefore, the process of preparing and joining the MEA with the bipolar plates can took several hours and need to be very meticulous to allow good contact between the MEA components and the cell to be leak-proof. The typical fuel cell assembly is illustrated in **figure 7 [24]**:

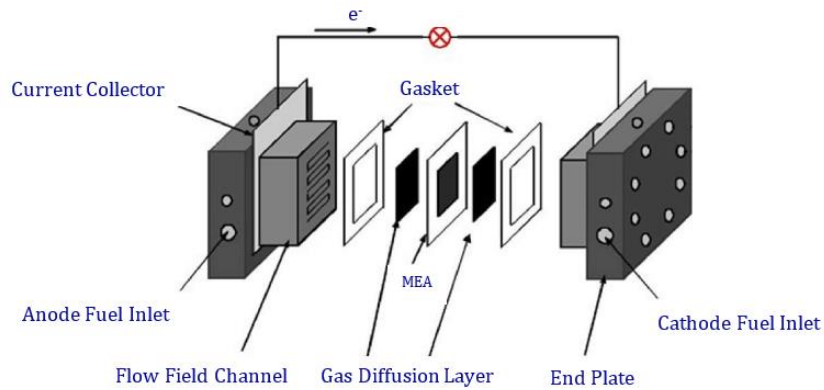


Figure 7: Fuel cell components assembly [24]

2.1.3 Water Management

One of the main technical challenges in the PEMFC is achieving and maintaining suitable water balance in the cell, which is crucial for optimal performance of PEMFCs. During its operation, there is liquid water being continuously generated in the cathode as result of the chemical ORR, see **equation (2)**, leading to an excessive amount of water in the cathode side.

There are four different fundamental water transport mechanisms through the membrane: the electro-osmotic drag (EOD), back diffusion (BD), generated water and hydraulic permeation (see **figure 8**).

The **electro-osmotic drag** transport water from the anode to the cathode, in which protons migrate through the membrane drag along water. The **hydraulic permeation**, driven by pressure, occurs mostly from cathode to anode, but is often negligible compared to EOD and BD.

Some fraction of this water will hydrate the membrane and improve its proton conductivity, enhancing the performance of the cell, as explained in the section 2.1.2; the other fraction of the produced water is transported to the anode by **back diffusion** or evaporates into the gas channel; however, this process occurs at a much slower rate than the water generation from ORR and electro-osmotic drag. This is the reason why water must be continuously or periodically removed from the cathode.

If the rate of removal is slower than the production and drag rates, water will accumulate in the cathode. This effect is called water flooding, which leads to the saturating the open pores in the GDL with water, blocking the transport of the oxygen to the catalyst layers anode and

cathode. Once it inhibits the reactants to reach the catalysts, GDL flooding drastically decreases the performance of the cell because it causes reactant starvation.

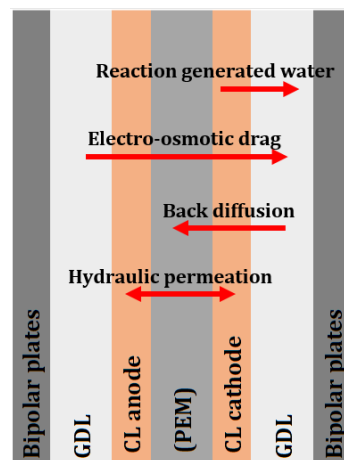


Figure 8: Water transport mechanisms through the membrane (Adapted from [23])

Furthermore, water flooding also occurs in the flow channels, lowering the performance by narrowing the flow cross sectional area in the flow channel, so called gas channel flooding. If the water removal rate is greater than the water generation and electro-osmotic drag rates, there is a water concentration gradient between the anode and cathode, leading to the back diffusion of water from the cathode to the anode: the membrane will be dehydrating. This is also leading to a decrease in the cell performance as it degrades the polymer and increases ohmic losses, caused by the increasing of the membrane electrical resistance. At low current densities, back diffusion and electro-osmotic drag rates are similar, however, at high current densities, electro-osmotic drag rate is higher than back diffusion, and water moves from the anode to the cathode, and may cause anode dry [25]. Summing, the presence of water is necessary to maintain the proton conductivity in the membrane; in the one hand, too much water drowns the cell, reducing its performance but in the other hand, deficit of water dehydrates the cell. Therefore, finding a proper water balance between the water production and removal for achieving the optimal performance of the cell is crucial. Understanding the water transport mechanisms in a fuel cell is the key for avoid flooding or in contrast, membrane dehydration.

2.2 Fuel Cell Monitoring

The performance of the cell is affected by numerous factors as previously explained. As well known by the scientific community, the electrochemical activity inside the cell is not homogeneously distributed, thus, a non-uniform current density and temperature distribution inside the cell is expected. This fact results in poor reactant and catalyst utilization and cell

performance degradation. To understand the influence of those factors in the cell performance, numerically calculated results are required to achieve a better understanding of the electrochemical reactions in the cell. A good insight can be attained from both theoretical and experimental work. Despite the good quality of today's simulation results, the simulation of current density and temperature gradients has shown the absolute need for additional experimental works, to validate simulation predicts and to reveal weaknesses in the models. Those results can lead to optimizing both components design and operating strategies to have more efficient and low costly PEMFC [26].

I. Current Distribution in a PEMFC

To optimize the cell performance, it is crucial having a uniform current density overall the active area of the cell. Current density gradients, keep up with non-uniform water production in the cathode, has a negative impact in the FC durability and reliability [27]. The factor who affects the most the cell performance is related to the unequal electrochemical reaction rate taking place at the MEA surface. The direct consequence is the poor reaction in those areas and poor catalyst utilization, accelerating cell degradation [28]. One technique to measure current distributions in the PEMFC is the segmented cell, an in-situ diagnostic tool. Segmented cell is identical to the traditional cell with the difference that the flowfield is segmented in smaller cells which are insulated from each other, allowing measuring their current independently. Freunberger et al [26] measured the current density distribution with a resolution smaller than the channel/rib scale. Wilkinson et al [29] tried to calculate the current distribution indirectly by correlating local temperatures with local current densities. Until now, studies on current density on the channel and rib scale are only theoretical [26]. Essentially, all authors report lower current production under the ribs in the high-current density range due to oxygen starvation, which can be partially overcome by forced convection.

II. Temperature Distribution in a PEMFC

The main sources of heat in a PEMFC are the entropic heat of the reactions, the irreversibility of the electrochemical reactions, water evaporation or condensation and ohmic resistance. Temperature is one of the key parameters affecting the performance, reliability [30] and lifetime of the fuel cells, since chemical reaction rates, proton conductivity, water transport phenomena, and other mass transport phenomena are strongly linked to the local temperature. Moreover, degradation of membrane [31] and electrode [32] are associated to the non-uniform temperature distribution and local hot spots caused by improper thermal management [33]. Temperature is also non-homogeneously distributed at the active area. Even small temperature gradients impact directly condensation regions and membrane

longevity. A high local temperature on the membrane surface will lead to its dehydration, thus, decreasing proton conductivity; a low local temperature may lead to flooding. The combined study of temperature distribution, heat management and current distribution in the cell enables a deeper insight into fuel cells phenomena.

2.3 Thermography

2.3.1 Infrared radiation

The transfer of thermal energy can occur through three different mechanisms: conduction, convection and radiation. Radiation refers to the waves of the electromagnetic field propagating through the space, carrying electromagnetic radiant energy. All forms of matter emit radiation [34]. Energy transfer by radiation results from the radiant emission by all objects with temperature above 0 degrees Kelvin, due to its molecules excitation energy. The amount of radiated electromagnetic energy of a body is proportional to its temperature. Thus, the bigger its temperature, the bigger its molecular excitation and then, the bigger is the intensity of the radiation emitted. In consequence, the temperature of an object can be determined by the intensity of the emitted radiation of its surface.

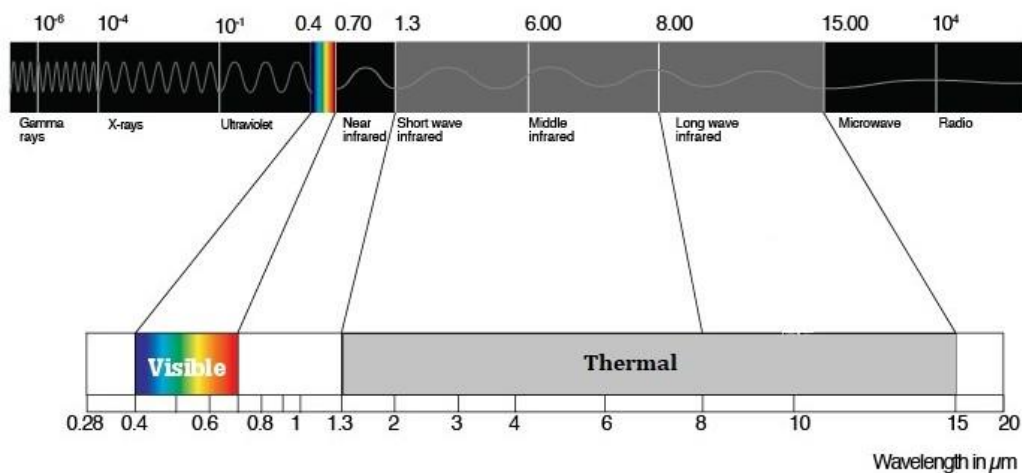


Figure 9: Wavelength range of the Electromagnetic Spectrum

Human eye can only see visible light (0.39-0.74 μm), a very limited part of the electromagnetic spectrum. Infrared energy is only a small part of the electromagnetic spectrum (**figure 9**) that also includes gamma-rays, x-rays, ultraviolet, visible light, infrared, microwaves and radio waves. At temperatures up to a few hundred degrees Celsius, most of the radiation is emitted in the infrared range. The key difference between thermal and near-IR is that thermal-IR is emitted by an object because atoms excitation while near-IR is reflected.

Blackbody Radiation

All bodies emit electromagnetic radiation as functions of its surface temperature and material properties. Theoretical objects with ideal radiative properties (emissivity $e=1$), called blackbodies, absorb all incident electromagnetic radiation, reflecting no radiation. Thus, all the radiation emanating from blackbodies is due to its surface temperature. At different temperatures and wavelength, blackbodies emit different radiation, see figure 10.

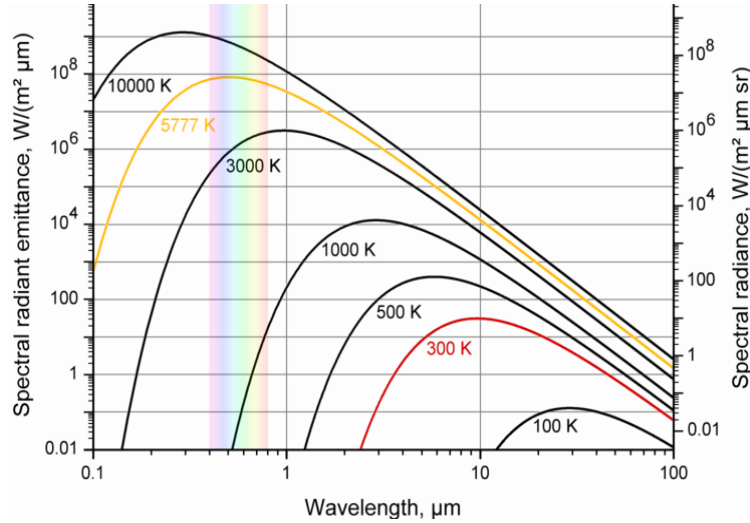


Figure 10: Blackbody radiation characteristic curves

As illustrated above, objects at near 5000 K (close to the temperature in the surface of the sun) emit radiation with a peak wavelength in the visible spectrum, while objects at earth temperatures, near 300 K emit the majority of their radiation at LWIR wavelength.

Planck Law, **equation (6)** describes the quantity of radiation at a specific wavelength emitted by a blackbody in thermal equilibrium as function of its surface temperature:

$$B_{\lambda}(\lambda, T) = \frac{2hc^2}{\lambda^5 \left(e^{\frac{hc}{\lambda K_B T}} - 1 \right)} \quad (6)$$

where B_{λ} is the spectral radiance of the blackbody surface ($\text{W}\cdot\text{m}^{-3}$), T the absolute temperature (K), λ is the wavelength (m), K_B is the Boltzmann constant ($\text{J}\cdot\text{K}^{-1}$), h is the Planck constant ($\text{J}\cdot\text{s}$) and c the speed of light in the medium ($\text{m}\cdot\text{s}^{-1}$). Planck's Law can be integrated to allow the radiance to be calculated over a defined range of wavelengths. For all wavelengths it's simplified to the Stephan-Boltzmann Equation (**equation 7**), that states that the thermal energy radiated per second per unit area by a blackbody is proportional to the fourth power of its absolute temperature.

$$\frac{P}{A} = j = \sigma T^4 \quad (7)$$

where P is the thermal energy radiated per second ($J \cdot s^{-1}$), A is the radiated area (m^2), j is energy flow density ($J \cdot m^{-2} \cdot s^{-1}$), σ is the Stephan-Boltzmann constant ($5.6703 \cdot 10^{-8} W \cdot m^{-2} \cdot K^{-4}$) and T is the absolute temperature of the object (K). For hot objects other than ideal radiators (blackbodies), the law is given by **equation 8**:

$$j = e\sigma T^4 \tag{8}$$

where the emissivity varies from $[0;1[$.

2.3.2 Infrared Cameras

In a general way, the operation of infrared and visible light cameras is similar. Like visible light cameras, infrared cameras form 2D images from the intensity of incident radiation on each pixel in the camera focal plane array. Both cameras need optical lens and similar electronics in order to transmit the data. However, the detection of infrared light, instead of glass lenses, must be made of IR transparent materials, such as germanium or silicon (see **figure 11**), to be transparent to infrared wavelength and opaque to other wavelengths. Also, the shape, size and composition of the sensor is different, to adapt to the order of magnitude increase in wavelength.

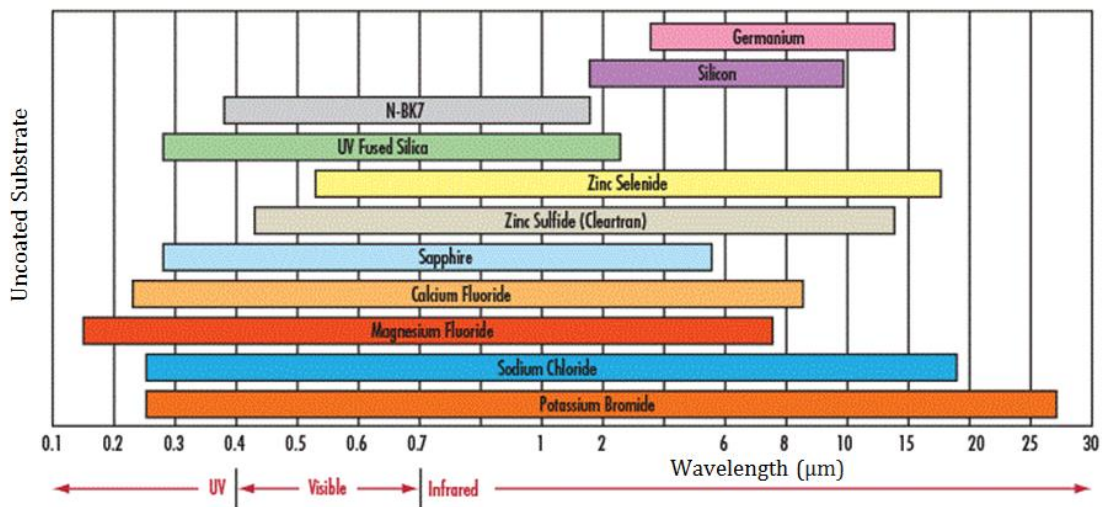


Figure 11: Transmittance range substrate of various materials

Despite the human eye can't see infrared radiation, these cameras are tools who determine the surface temperature of an object by measuring the intensity of the emitted radiation of its surface. They commonly detect infrared radiation in the range of the spectrum 6-8 μm MWIR (middle wavelength Infrared) and 8-15 μm LWIR (long wavelength Infrared).

Infrared cameras can be divided into two classes accordingly they use quantum or thermal detectors. Quantum detectors are significantly more accurate but require an external cooling system and they are more expensive. The ones who use thermal detectors require no cooling system and use a “microbolometer” detector to measure the incident radiation. These last, are the most common detectors used in commercial infrared cameras, and the one who are used in this thesis.

A Germanium lens focuses the infrared light emitted by the object, then this focused light is scanned by a phased array of IR-sensor elements which creates a very detailed temperature pattern called thermogram. The thermogram created by the sensor is translated into electric impulses that are sent to a signal-processing unit that translates the information from the elements into data for the display. The signal processor sends the information to the display, where it appears as colors depending on the IR emission intensity of the object. From the combination of all the impulses from all the elements an image arises [35], see **figure 12**.

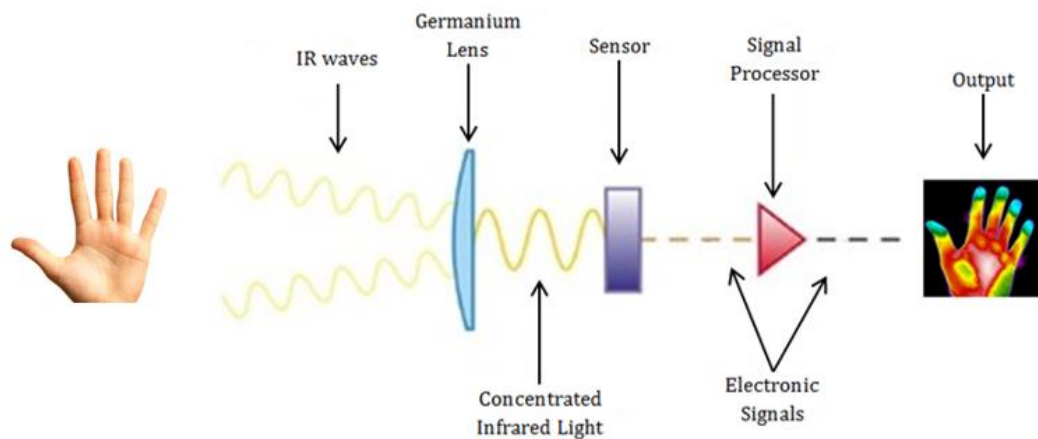


Figure 12: Thermal cameras principle of work

Thus, thermography is a non-interfering method used to measure surface temperatures of the bodies. Some characteristics related to thermal cameras are temperature range, thermal sensitivity, thermal resolution, spatial resolution and accuracy. Temperature range is related to the sensor’s technology to detect waves along a certain range of temperature. Thermal sensitivity is the ability to recognize changes between energy levels, expressed in terms of temperature. The high sensitivity, the lower temperature differences it can distinguish. Spatial resolution is the number of pixels of the image, given by a matrix of numbers. Accuracy is how close the object temperature is to the real temperature, usually $\pm 2\%$ [36]. The application for this devices arose from the army after World War II, however nowadays they are used in domains as navigation, aviation, automotive, geological and wildlife survey, power line maintenance, firefighting, entertainment, medicine [37], etc.

3 Setup

3.1 Fuel Cell and Test Bench

This section comprehends sub-chapters: I) anode, II) cathode, III) assembly and IV) test-bench. The design of the cell used for developing this study is quite different from a conventional PEMFC. The idea of looking inside the fuel cell through an infrared window to access to local temperatures demands a completely new design, first started by Torsten Knöri at DLR Stuttgart. The test cell used in this study has 25 cm² of active area.

I. Anode: The Segmented Cell technology

Due to an inhomogeneous electrochemical activity inside the cell, produced by inhomogeneous reactants distribution, stoichiometry of the fed reactants, process cell temperature, inlet relative humidity of the reactants and other factors, there is an inhomogeneous water vapor formation inside the membrane. To visualize the current density distribution inside the cell, local current measurements were performed. For that, DLR patented a printed circuit board (PCB) - **figure 13** - that allows to obtain local current distribution, within 49 segments, and access the temperature in 6 positions. Instead of measuring the integral current from the whole area of the cell, it measures the internal resistance in each segment, and thus, local current density can be achieved. This is more accurate when giving information about the local electrochemical activity [38].

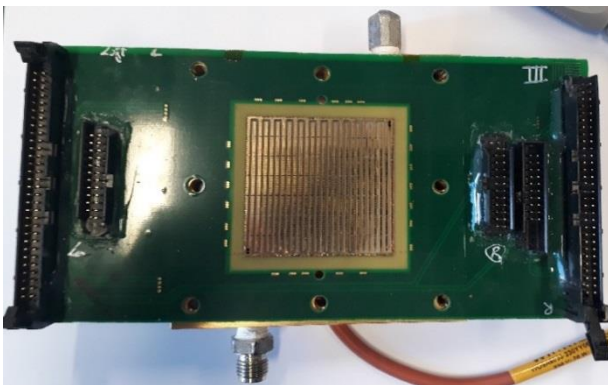


Figure 13: Printed circuit board

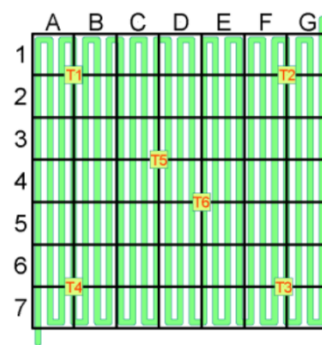


Figure 14: Flowfield scheme in the PCB

This PCB embodies the flowfield plate whose only purpose here is to conduct electrons and clamping the cell. In **figure 14** it is possible to observe three aspects of the PCB: the single serpentine flowfield, the segmentation of the cell in A to G rows and 1 to 7 lines matrix, in a total of 49 segments, and the 6 temperature sensors with their positions. The active area is 5 cm width x 5 cm length, performing 25 cm².

II. Cathode side: Plate, flowfield and transparent window

To visualize what is occurring during the reaction in the cathode, a window transparent to infrared radiation was placed in the center of the cathode bipolar plate (**figure 15**). Thus, the cathode plate could not embody both the IR window and flowfield; in consequence, flowfield became an independent component from the cathode plate, see (**figure 16**).

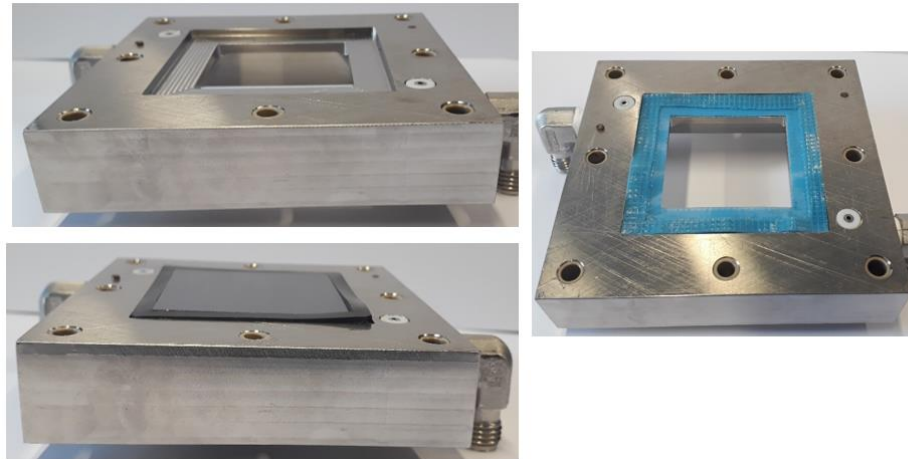


Figure 15: Framed Cathode plate for the IR transparent window

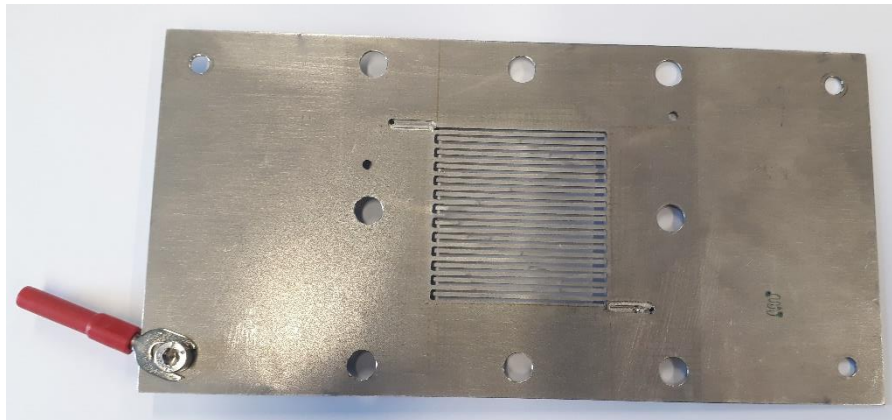


Figure 16: Individual flowfield plate with single serpentine configuration

III. Assembly

As illustrated in **figure 17**, the components assume similar positions as in the traditional assembly, represented in figure 7, despite their design is quite different especially concerning some of the components. A gasket was placed in both sides of the MEA, both to seal it and to avoid a short-circuit. A polyethylene thin film was placed between the flowfield and the cathode bipolar plate, to decrease air leakage through the frame. Both single serpentine flowfields were placed vertical and in counter-flow configuration. To seal the cell, a diagonal torque was applied with small increments of 0.2 N·m until 2.2 N·m. The small increments are

critical to avoid the unbalanced tensions to rise above the tensile strength of the silicon window. The assembled fuel cell can be seen in **figure 18**.

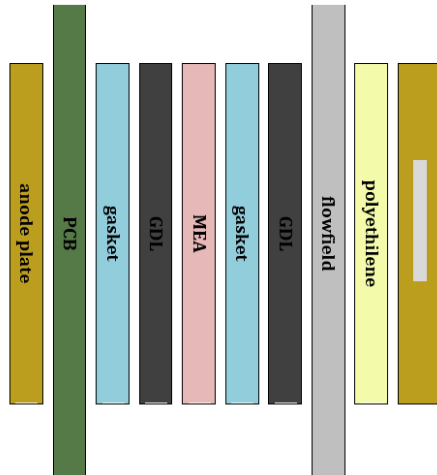


Figure 17: Fuel cell scheme assembly

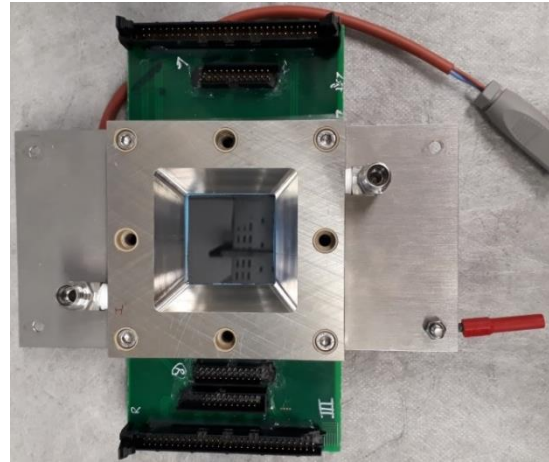


Figure 18: Fuel cell assembled

IV. Test- Bench & Software

After assembling the cell, this was put to run in the test bench (**figure 19**). The current collectors were placed at anode plate and at cathode. One sensor of temperature was placed in the anode and another in the cathode. The PCB was then connected to the data acquisition system. Four 4×0.5 cm heaters were placed in the lateral surfaces of the cathode plate, supplied by a power supply. The cell was conditioned during two hours in potentiostatic mode at 0.6 V and then changed to galvanostatic mode for two more hours, after reaching a stable potential. The operating conditions for a 25 cm² active area cell depend on each experiment and will be detailed further. The control software was Simatic WinCC. For the segmented cell, an in-house software developed was used. The optic system was assembled in an independent bench and placed over the cathode side. The focal plan was adjusted for the most active area within the segmented cell. The optical system has an independent software, detailed in section 3.2. The systems identified with blue and red rectangles in figure 19 are the fuel cell and optical system, respectively. A closer view of the setup is shown in **figure 20**.

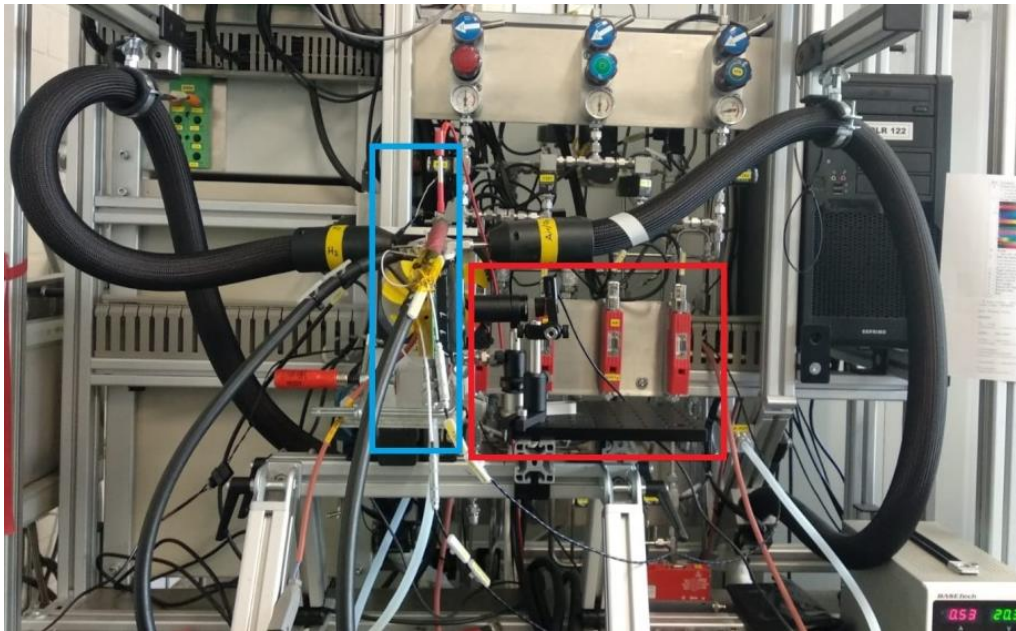


Figure 19: Test-Bench outer look

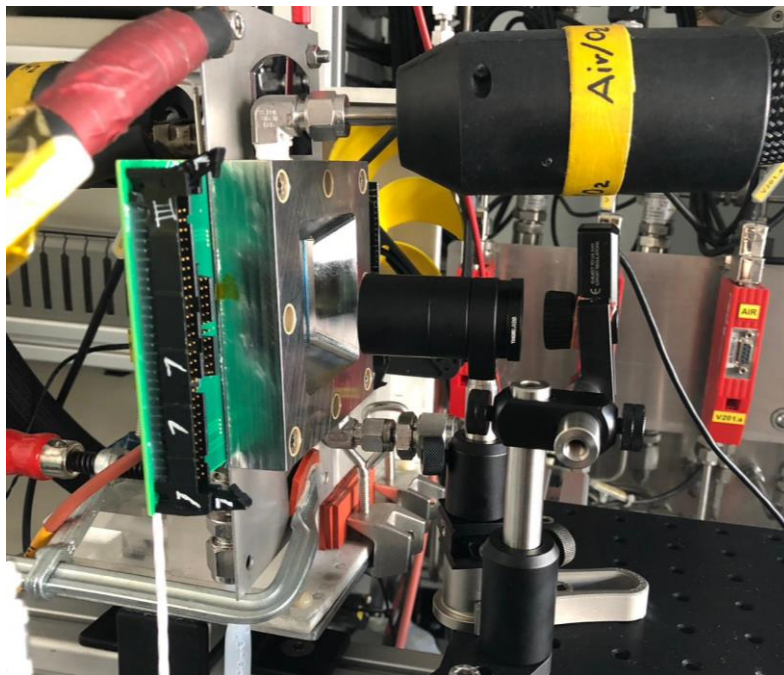


Figure 20: Close look into the systems interaction

3.2 IR camera before being adapted

The infrared camera used for this study was a Seek Thermal CompactPRO, see **figures 21** and **22**; the specifications of the camera are shown in the **table 2**.



Figure 21: Seek Thermal CompactPRO [39]

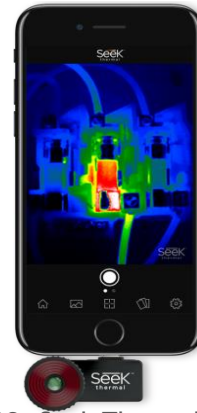


Figure 22: Seek Thermal in use

Table 2: Seek Thermal technical specifications

Specifications	
Thermal sensor (pixels)	320 x 240
Field of View	32 degree
Temperature range (°C)	-40 330
Thermal Sensivity (mK)	< 70
Spectral Range (Microns)	7.5 - 14
Lens Material	Chalcogenide
Microbolometer	Vanadium Oxide

This device was developed for systems iPhone® and Android™, with the promise of transforming the smartphone into a professional thermal imaging tool. It uses the power of the smartphone, recording images and videos. There is an app to run the tool, called “Seek Thermal” and it is available at the Google Play site with no costs. The main applications for this device, accordingly to the brand, are to detect energy loss caused by air leaks, damaged insulation, electrical faults and leisure. The actual price in the official website is \$ 499 [39]. The camera comes with a fixed 32° field of view lens, which is satisfactory for general thermal inspection, but it is a disadvantage when used for close-up works, which is the purpose of this thesis. An in-house software to run the camera was developed by Peter Mahnke, with more adequate functions than the Seek Thermal app.

The further work was dedicated to develop a magnifying converter for this camera and to explore the limits of this low-cost solution for thermography in fuel cell research.

3.3 Materials used for (further) development

To enhance the quality of the thermal imaging, we must first know that camera performance includes careful analysis of much more parameters than just the spatial resolution. As previously explained, a thermal camera is an image converter, converting radiant thermal energy to a visible image called thermogram. By exploring the potential and limitations of thermal IR applied to fuel cells, we are contributing to the advancement of the field. The used materials are described below and the reason for their meticulous choice is explained in detail.

3.3.1 Lenses & other elements

A lens is an optical system consisting of two or more refracting interfaces where at least one is curved. Generally, the non-planar surfaces are centered on a common axis. These surfaces are mostly frequently spherical segments, and often coated with thin films to control their transmission properties. They can be classified either as thin or thick lenses, according to their thickness to radius ratio.

Different combinations of lens were used to achieve a considerable magnification of the area of study, the ribs and channels inside the cell. The available lenses are listed on **table 3** and other complementary elements listed on **table 4**. All the optical materials described in tables 3 and 4 were provided by Thorlabs, except lens ii (Ge meniscus), that was provided by Edmund Optics.

Table 3: Available set of lens

ID	Shape	Substrat	AR coating	AR coating range (μm)	F.L. (mm)	un.	\emptyset (mm)	Refraction Index
i	Plano-convex	Ge	-	-		4	25	4.003
ii	Meniscus	Ge	✓	8.0 - 12.0	25	2	25	4.003
iii	Plano-convex	ZnSe	✓	7.0-12.0	50	1	25	2.403

Table 4: Complementary elements for the optic setup

	Material	Size (mm)	un.	Brand code	Features
Iris diaphragm	Spring Steel Leaves	Ø0.8-Ø25	2	SM1D25	-
		Ø0.8-Ø12		SM1D12	
Optical breadboard	Anodized Al	200×200	1	MB2020/M	Black Surface with Low Reflectance
Lens tube spacer	Anodized Al	Ø25	2	SM1S20	Length Range: 25.4 - 88.9 mm
Tube w/ rotating adjustment	Anodized Al	Ø25 mm	1	SM1V15	Adjustment Range: 2.8 - 36.1 mm
Fixed Lens Mounts	Al	Ø24	3	LMR1/M	-

Germanium Lens (i & ii)

Germanium (Ge) is a chemical element with atomic number 32. It is a lustrous, high-density, hard, grayish-white metalloid in the carbon group. Pure germanium is a semiconductor and has good thermal conductivity. It is one of the most important high refractive index materials for optical coatings due to its wide transparent region in the IR band and low optical dispersion. Ge blocks UV and VIS wavelengths but allows IR in the 1.8 to 14 μm spectral region (**appendix 1, figure 23**). Due to its optical and structural properties (**appendix 1, table 5**), it became one of the most important materials in the micro-electronic and optical industries. Ge films are used for thermal imaging, FLIR (Forward Looking Infrared) and FTIR (Fourier Transformed Infrared) spectroscopy systems, alongside other analytical instruments. However, it must be coated with anti-reflection agents. Particularly, a very hard special antireflection coating of diamond-like carbon, refractive index 2.0, is a good match. It is especially used as the front optic in thermal imaging cameras working in the 8 to 14 μm .

Germanium lens i from table 3 is a non-coated lens positive meniscus shaped, with two spherical surfaces, S1 and S2. Due the inexistence of the AR coating, this lens has worse performance than the Germanium coated, thus, it was not used in the final setup.

Germanium lens ii from table 3 is an anti-reflective (AR) coated lens positive meniscus shaped, having two spherical surfaces, S1 and S2. This lens has an asymmetric structure with one face shaped as convex radius, while the opposite face is slightly concave (**appendix 1, figures 24-26**). A meniscus lens is thicker at the center compared to the edges; in particular, positive meniscus is that lens that has a greater curvature radius on the concave side of the lens than on the convex side, enabling the formation of a real image. They are usually used with another lens to produce an optimal system having either a longer or shorter focal length

than the original lens. They can be positioned after a plano-convex lens to shorten the focal length without decreasing optical performance [40].

Zinc-Selenide lens iii from table 3 is also AR coated, with plano-convex shape (**appendix 1, figures 27, 28**). Its refractive index is 2.4 and is a common choice to IR applications due to its low absorptivity at IR wavelengths. ZnSe allows transmission on IR light in the band 0.6-21 μm (**appendix 1, figure 29**). It is a relatively soft material and scratches easily. Its low absorption avoids the thermal runaway problems of germanium, being usually more expensive than this. Due to its high refractive index, an AR coating is desirable if a high transmission is required. More details about ZnSe can be found in the appendix 1, **table 6**.

Iris diaphragms:

Iris are used to limit the amount of light transmitted to the camera sensor to prevent oversaturation, a lot like the pupils in our eyes, changing according how much light we need to capture. These optical components feature a series of smooth, thin leaves arranged to form a circular aperture in the center, opening and closing, controlling the amount of light that reaches the sensor, enhancing the quality of image. A larger aperture, see **figure 30** captures more light than smaller aperture, however, this is not the only thing that aperture changes: the other important effect is *depth of field*, DOF, or the area that is in focus in the image. The basic rule is: reducing the aperture diameter (increasing the f-number) increases the DOF because the only light travelling at shallower angles passes through the aperture. Because the angles are shallow, the light rays are within the circle of confusion for a greater distance. By just adjusting iris aperture, we have one of the best tools to capture a good sharp image. Aperture is often written as an *f*-number that means a fraction of how much the iris is closed, for example *f*/2 means aperture of one-half, which is much larger than for example *f*/16. This *f* number is the focal length. When we substitute the focal length into the fraction, we are solving the diameter of the aperture blades in the lens [41].

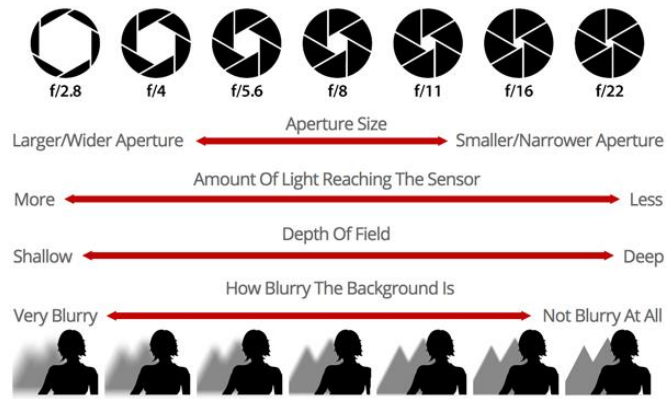


Figure 30: Size of the aperture and depth of field [41]

Anti-reflective coating (AR):

AR coating is an optical coating applied in the lenses surface to minimize surface reflection, improving lenses efficiency by losing less light due to reflection and increasing the contrast of the image by eliminating the stray light. With no AR coating, 4%¹ of the light is lost in each optical surface due to reflection. As an example, if we use three uncoated lenses in series, 4% light loss occurs at each of the six optical surfaces, resulting in a total loss of 21.7% of light [42]. AR coatings consist of multiple layers, alternating between high and low refractive index materials, deposited on the substrate via electron-beam deposition. The layer thickness is optimized to produce destructive interference between reflected waves and constructive interference between transmitted waves, resulting in an enhanced performance in a specified wavelength band.

¹ 4% is an approximate value that varies greatly with material and angle of incidence.

3.3.2 Infrared Transparent Window

Silicon (Si) has the diamond crystal structure. Its bravais lattice is FCC and wafers are usually made on [100] crystallographic plane, which need to be cut off-axis at the appropriate angle. Six wafer samples of Si with $1500 \pm 25 \mu\text{m}$ thickness and 4 inches diameter were cut in a Buehler IsoMet 4000 precision saw with size $5 \times 5 \text{ cm}$. The Silicon frame was placed in the center of the cathode plate, as previously seen in figure 15. Silicon was chosen due to its optical properties: at 300 K, its infrared refractive index $n(\lambda)$ is 3.42 and its transmission curve can be seen in **figure 31** showing that it transmits IR wavelengths between $1.2\text{-}8 \mu\text{m}$ but is opaque to visible light. Transmission is given as a percentage of the incident light plotted against the wavelength. Despite the best option due to its transmittance and refractive index would be Germanium, the ordered wafers were not available in time for this work. More details about Si can be seen in **appendix 1, table 8**. Four Si windows were broken

during experiments, two of them due to the wrong cutting-off angle, and two while assembling due to excessive torque. The wafers used were provided by MicroChemicals GmbH.

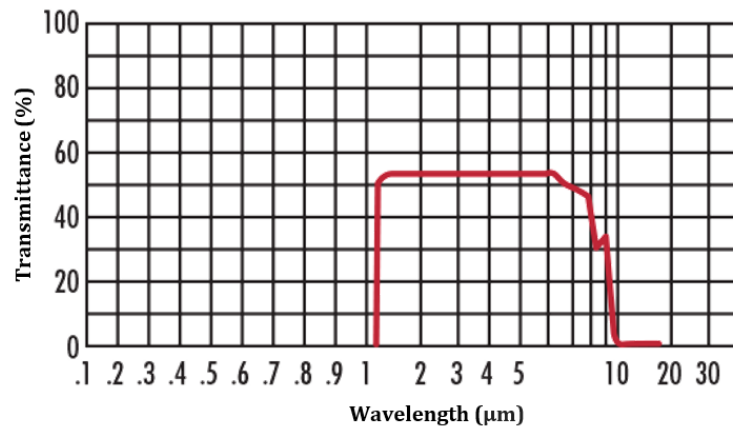


Figure 31: Silicon transmittance curve

4 Results: Applications & limitations

4.1 Modifications and Improvement of the FC

The fuel presented in the section 3.1, (figures 15 and 16) is the result of a continuous development, since the first sketches were trials to understand what necessities the components should have to mechanically fit in each other and properly perform its function.

The first version of the cathode plate was built in house in a 3D printer, thus, made of Polylactic acid polymer (**appendix 1, figure 32**); however, due to mechanical deformations when attaching the gas feeds and outlets (**appendix 1, figure 33**), a necessity for a substitute material emerged: the stainless steel plate, also made in house was born (**appendix 1, figure 34**).

The first version of the flowfield was a sketch (**appendix 1, figure 35**) with some problems when conducting the gases from the inlet to the GDL, (**appendix 1, figures 36 and 37**). There was the necessity of creating a path for the gases, from the whole inlet to the GDL: the final version is the one in the figure 16. The difference between them is that the 2nd version has the stainless steel 1cm path from the whole inlet to the GDL. To enhance the diffusion of the gases to the GDL, a small area of GDL was placed in the previous mentioned path (**appendix 1, figure 38**). After cell assembling, these small pieces intruded the flowfield path, blocking it (**appendix 1, figure 39**) and thus, the torque had to be reduced. To block the flowfield sliding, two pin panels were inserted in the cathode plate (**appendix 1, figure 34**) and two holes were made in the flowfield (see again figure 16), fixing the flowfield into the plate.

To cut the Silicon, a diamond pen scriber was tried (**appendix 1, figure 40**) but due to Si thickness of 1500 μm , it was not possible to cut the windows with this technique. The IR transparent window wafers were cut in a Buehler IsoMet 4000 precision saw, along its crystallographic plane.

The new cell components were ready to operate and the cell was functional, nevertheless there was a considerable oxygen gas leak in the window. To minimize the leakage, a combination of materials to put in the plate frame as sealing was tested. A set of Viton™ rubber sheets with different thicknesses was tested (**appendix 1, figure 41**). A torque of 3 N·m was applied but the Silicon window shattered. After several tests combining layers of Rubber Viton™, layers of gasket and Viton combined with gasket, the actual version is a layer of 1.08 mm thickness Viton™ and 3 layers of gasket, to decrease the hardness of Viton and avoid Silicon break. The leakage was significantly reduced but was not completely eradicated.

4.2 Thermography

4.2.1 Intrinsic magnification/full view

The first IR observations of the fuel cell consisted in removing the spherical lens of the camera and observing directly the cell. The idea of removing the lens was automatically declined because the sensor was not protected, and thus the adjacent experiences were done with the intrinsic lens of the camera. It is estimated that the focal length of the camera lens is around 6mm. The next observation of the cell was simply pointing the Seek Thermal into the channels and ribs. The operatory conditions for the 25 cm² active area cell were set in the Simatic WinCC software and are summed up in **table 9**. For this experiment, two alternating cycles of 10 minutes each varying the inlet humidification were performed. The images were collected when a cycle of 50-50% RH finished and a cycle of 100-100% RH started.

Table 9: Operatory conditions

Parameter	Value
Anode flow stoichiometry	1.5
Cathode flow Stoichiometry	2
Cell temperature, (°C)	60
Gas inlet humidification (cathode/anode) (%)	100-100 vs 50-50
Anode inlet pressure (bar)	1.1
Cathode inlet pressure (bar)	1.1

The emissivity of the stainless steel flowfield is close to 0.77, and the emissivity of carbon close to 0.97, allowing distinguishing between channels and ribs. **Figure 42** is a chronological sequence of a zoom-in section of the active area, between the 22nd and 31st seconds. By the sequence in this figure, it is possible to see the evolution of the water formation by means of the growing bars (light green) in the channels marked with boxes. The contrast was adapted to printed media. This sequence is much easier to observe when the sequence of the images is seen at a screen.

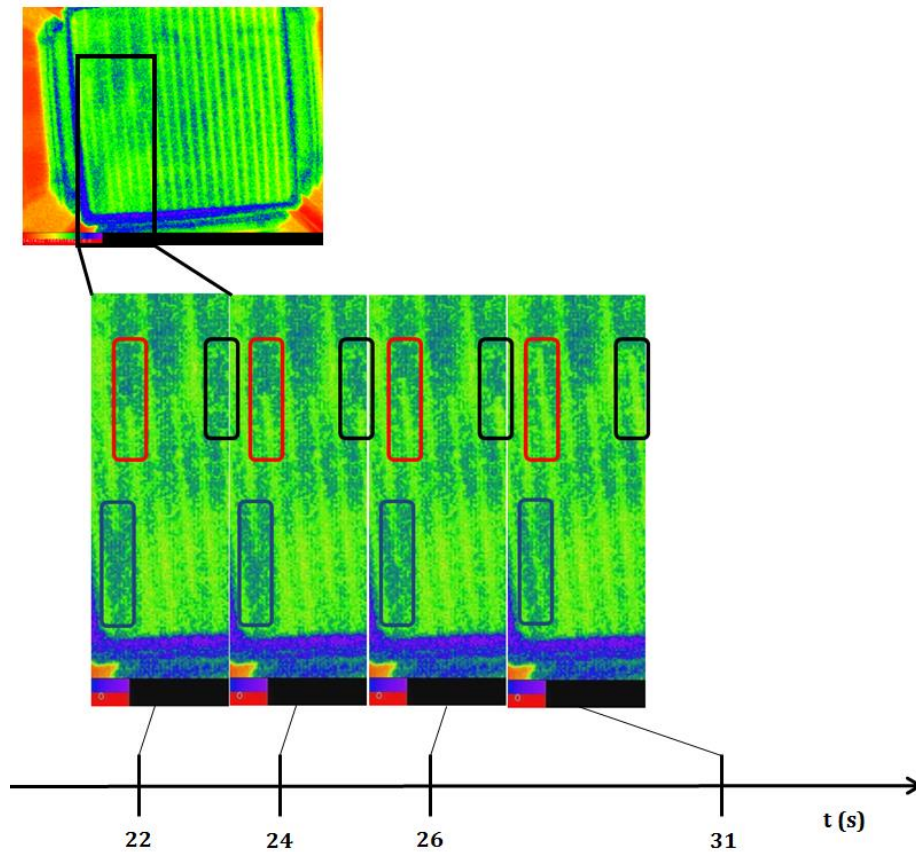


Figure 42: Water accumulation in the channels

The resolution of the Seek Thermal is 360 x 240 pixels. The flowfield embodies 25 channels and 24 ribs, each one with 1mm, composing 49 mm lateral size. The total image corresponds to 360 pixels in the lateral side. The image that corresponds to the flowfield area is 70% of the size of the total image. Thus, intrinsic resolution is 5.15 pixels per channel. This magnification for each channel and rib is not enough to have a good perception of what is occurring locally in the channels. Therefore, the following works goal is trying to achieve a better resolution per channel.

4.2.2 Magnifying Setup

In order to describe the magnification properties of an optical system, let's suppose an object which is either self-luminous or externally illuminated and imagine its surface as a large number of point sources, each emitting spherical waves, diverging from the point source S . Now envision the situation where a point source in the vicinity of some arrangement of reflecting and refracting surfaces representing an optical system. From the infinity of rays emanating from S , only one will pass through an arbitrary point in space. Even so, it is possible to arrange for an infinite number of rays to arrive at a certain point P , **figure 43 a**). Thus, the energy of a cone of rays coming from S that reach P , is said to be the *perfect image*

of S (apart from losses due to reflection, scattering and absorption). The waves could arrive to form a finite patch of light or blur spot about P - it would be still an image of S but no longer a perfect one.

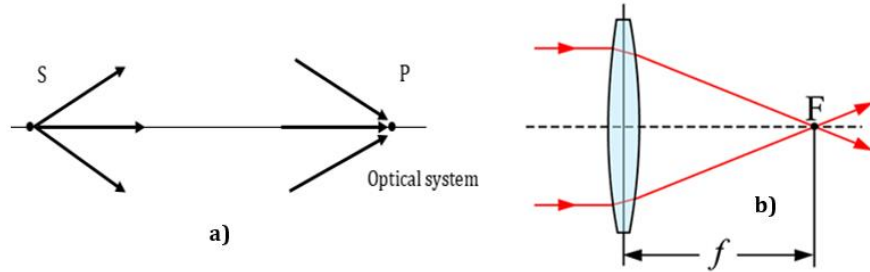


Figure 43: a) Converging and diverging waves; b) focal point and focal distance

The main function of a lens is to collect parallel rays of light and converge them into a single point of focus, so they can be recorded. This point is called the focal point F. In the **figure 43 b)**, the parallel rays of light entering the lens are represented by the two red arrows. The focal length is the distance between the center of the lens and the focal point. Without a lens to focus the light for the sensor, the image will be blur. In the thin-lens model, **figure 44**, the position of a point P in front of the lens is related to the position of the points focused image P' behind the lens by the **equation (9)**. The magnification of a single lens is given by **equation (10)**:

$$\frac{1}{f} = \frac{1}{d_o} + \frac{1}{d_i} \quad (9)$$

$$M = \frac{h_i}{h_o} = -\frac{d_i}{d_o} \quad (10)$$

Where f is the focal length of the thin-lens, d_o is the lens-to-object distance, d_i is the lens-to-focused image distance, h_i is the image height and h_o is the object height. If we multiply equation (14) per d_o results in the **equation (11)**:

$$\frac{d_o}{f} - 1 = \frac{d_o}{d_i} = \frac{h_o}{h_i} = \frac{1}{M} \quad (11)$$

For a given focal length of the system, magnification increases with the decreasing of lens-to-object distance, allowing us to put the camera very close to the cell.

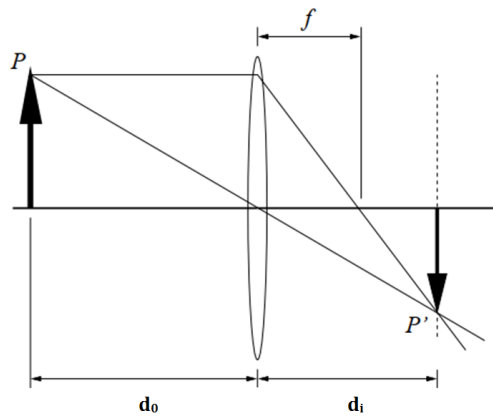


Figure 44: Basic thin-lens image-formation model

The following work consisted in experiments to increase the magnification of the system. To achieve that, a combination of several lenses was tested. The next step consisted in adding a germanium coated meniscus shaped lens (lens ii, table 4). A magnification was achieved, figure 45, but the image was not shaped.

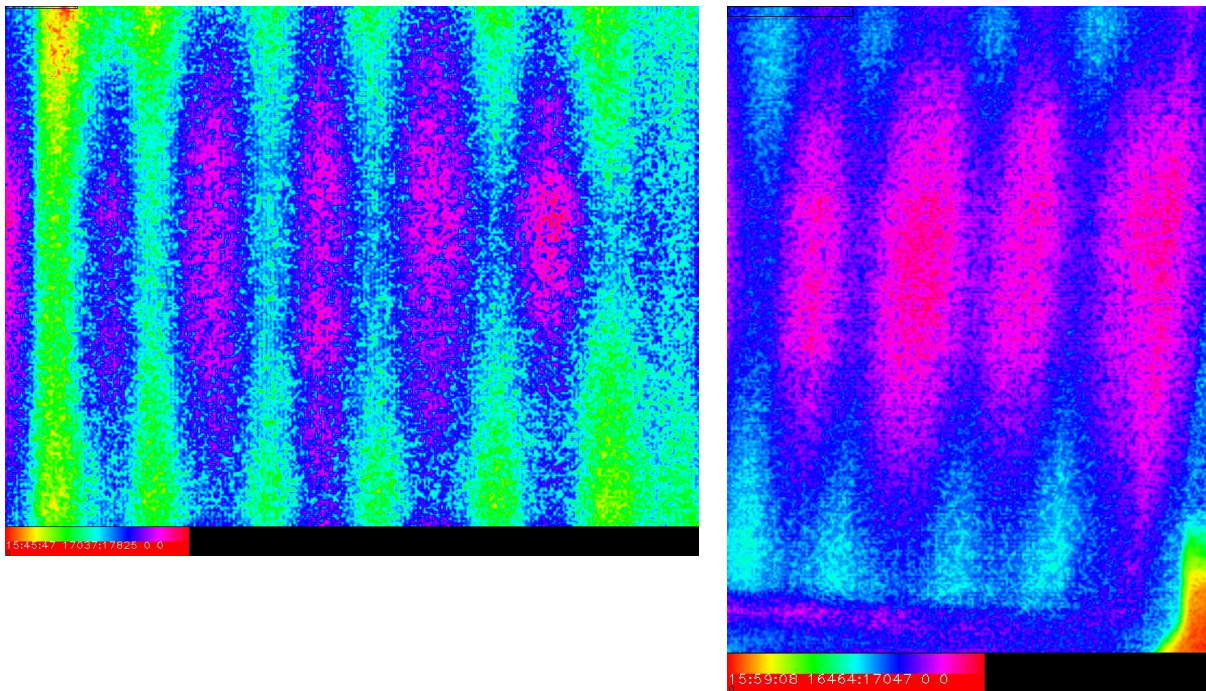


Figure 45: Ge lens magnifying channels and ribs

In an ideal system, all the rays of light coming from an object would converge to the same image plane creating a clear image, but some influences called aberrations occur, converging different rays to different points, creating this “distorted” image above. The pictures show channels and ribs magnified but for this magnification with the germanium lens, the channels and ribs seem blurred. As the center-to-center separation between the channels is not constant, the optical resolving power of the system became a limiting factor whether the

lines are clearly divided. Some examples of aberrations and respective correction can be seen in **appendix 1, table 10**. For the images in the figure 45, the resolution was not calculated due to the unsharpness of the image that would create inaccurate values.

To improve the sharpness of the image, a coated lens made of Zinc-Selenide was added (lens iii, table 3) between the Germanium and the camera lens, see **figure 46**. The fuel cell (1) is the object of study of the optical system, constituted by the meniscus germanium lenses (2), the plano-convex zinc-selenide lens (3), iris diaphragm (4) and Seek Thermal lens and sensor (5), all in series.

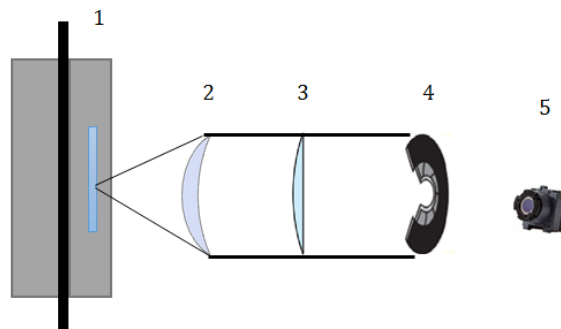


Figure 46: Optical system scheme

A set of two objective lenses were placed close to the Silicon window (2) and (3); these lenses are the most complex components in the system, collecting IR light from the cell, spreading out the light rays from the fuel cell, thus, magnifying the image. Then, the lenses send this real, inverted and magnified image to the Seek Thermal lens that also magnifies the image, sending it to the sensor. All the lenses contribute to the overall magnification.

The following experience ran with the same operatory conditions as without magnification (see table 9) but the relative humidity was set 100%-100% (anode and cathode) and suddenly set to 0-0% RH and the temperature was stable in 60 °C and changed to 90 °C. The resulting sequence of thermograms can be observed in **figure 47** and the first image in the sequence occurs 6 minutes and 8 seconds after changing the operatory conditions. The interval of pictures is between 9:28:01 and 9:28:40. In terms of magnification, the image corresponds to 360 pixels in the lateral size. The width of a rib corresponds to ~ 12% of the image. Thus, the total magnification achieved by the optical system is near to 44 pixels per channel.

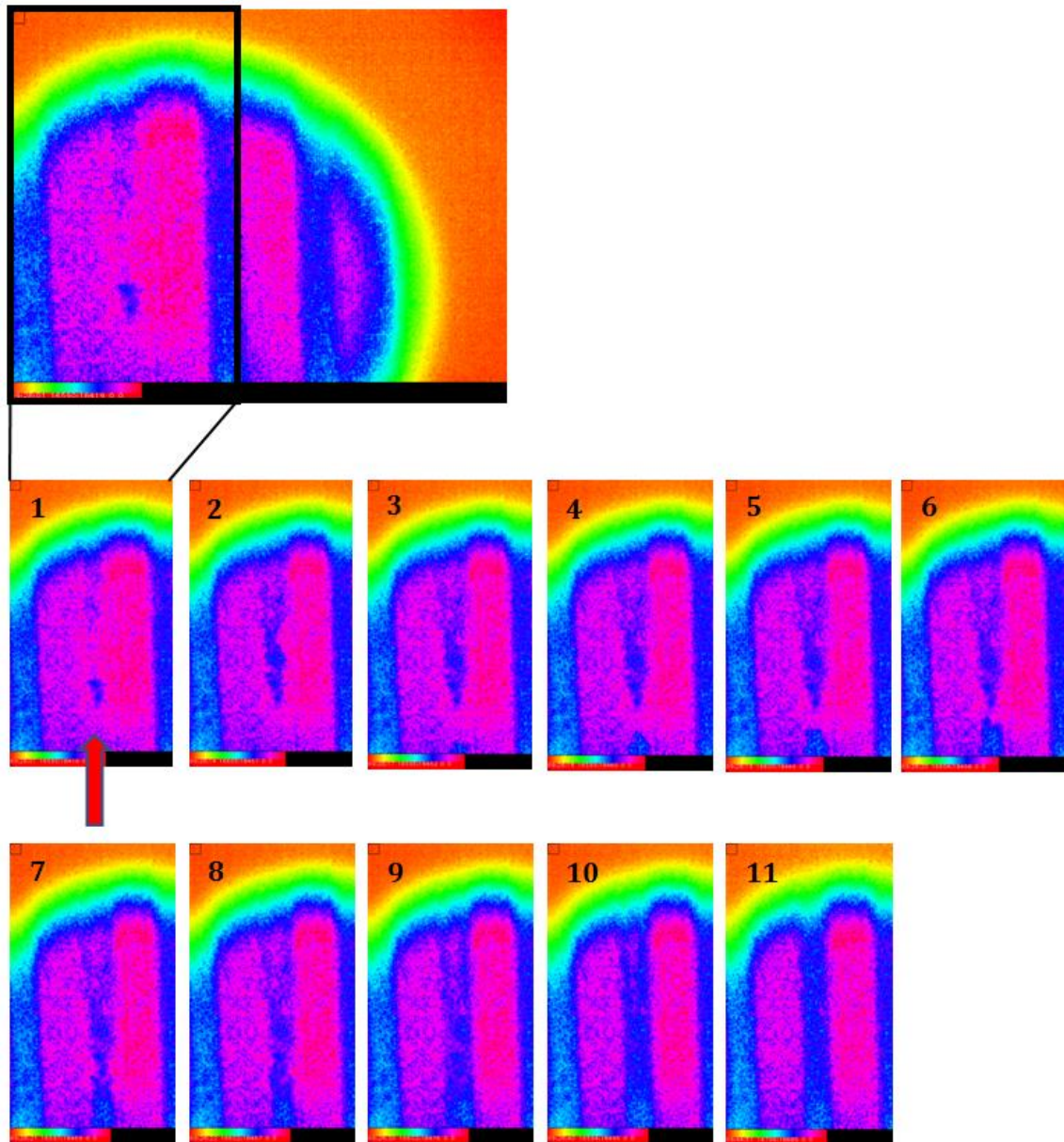


Figure 47: Sequence of images showing water removal mechanism in one channel

The pink color corresponds to the ribs and the blue to the dry channels. The channel under observation is signalized with the red arrow. The water filled the channels, that do not show a contrast to the ribs, become dry and change from pink to blue, in this color scheme. Notice that along the sequence of thermograms, the channel become sharper due to water removal. It is known that water is produced in the cathode catalyst layer, passes through the GDL and then enters in the flow channel. Thus, water droplets emerge on the surface of the GDL. In this sequence, we see generally that water is removed from the central axis of the channel into the direction of the ribs (see figure 47, thermograms 5-8), what lead us to think intuitively that there is more quantity of water near the walls, being the last area where drying occurs. This is consistent with the model for water condensation under the ribs (see

appendix 1, figure 48), that states that there is higher quantity of water emerging from under-ribs. Also, this sequence of images is consistent with the idea that drag force created by the air flow passing by the channels is removing water.

For the next experience, at the same operatory conditions as table 9, the relative humidity was initially 0-0% and the temperature of the cell was stable in 80 °C. Suddenly the temperature was changed to 95 °C. The first thermogram in **appendix 1, figure 49** was taken 2 minutes and 31 seconds after changing the temperature and the interval of the pictures is between 15:17:31 and 15:19:49. It is possible to follow the water removal from the channels starting at the 1st thermogram in figure 48 (image 1) until the last (image 36). Notice that in the image 2 it is possible to observe the first dry area in the signalized channel, starting randomly in a section of the channel. In the image 6 is visible that the upper part of the channel starts to dry. From images 2-24 it's possible to observe that the water removal in this channel is indiscriminate, and in the image 24 this channel is almost dry. In parallel, in the image 4 we see that the signalized channel starts also to dry from the bottom. The same channel, in the image 10 shows that there is a dry area near the upper part of the channel. The drying process continues until the image 25. Looking to the image 26 we observe that the signalized channel shows some dry areas in the middle of the channel, drying until image 36. It seems to be a random removal of droplets of water, with no preferential driving force to the drying process. Now, looking to the image 33 we see that the signalized channel starts to dry from the bottom, and the next thermogram shows that drying occurs at the same time from the bottom and from the upper part, towards the center of the channel. Contrary to what we observed in the **figure 47**, water removal here it is not happening from the central axe of the channel in direction of the walls but it seems that water is being removed from any arbitrary area of the channel. This leads us to the point where we know that water removal is a combination of several mechanisms, combined with heat management inside the cell. The mechanism of water removal from the GDL surface is strongly determined by the air velocity in the gas channel. If the gas flow velocity is high and the droplet is small, water is removed by the drag force exerted by the gas flow. On the other hand, if the gas flow velocity is low and the droplets have size similar to the channel dimension, capillary interactions with the channel sidewalls are dominant. A single droplet in the surface of the GDL has the following forces acting in it: drag force F_{drag} , viscous friction F_v , and surface tension force F_{ST} , see **figure 50**:

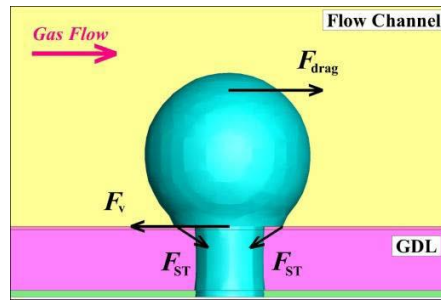


Figure 50: Schematic of the forces acting in a water droplet

Drag force created by the air flow passing through the water droplet is the driving force to push the water droplet forward, what is coherent with what is visualized in the figure 47. So, contrarily to the mechanism of water removal in figure 47, the mechanism here seems to be different, with some areas drying randomly in the channel, and some remaining wet. In this experience, some spots hold water drops of water for longer in the GDL, meaning that surface tension is high, keeping the droplet retained in the GDL surface, instead of being dragged with the air flow. The surface tension force is related to the surface tension coefficient, droplet shape and angle of contact of droplet and flowfield walls. All these forces are affected by different operatory conditions and design parameters, which results in a complex mechanism system to understand the dominant mechanism on water removal.

4.2.3 Iris Aperture effect

With the iris totally open, all the rays coming from the lenses are transmitted to the sensor of the Seek Thermal. With a smaller aperture, we are limiting the amount of rays that are sent to the sensor, producing a sharper and narrower image. The effect that happened with different iris apertures is the one exemplified in **picture 51**. With the iris totally open, with higher angle of view, (figure 51 a)), it is possible to observe a shallow deep-of-field because light rays partially are obstructed by the rib; by closing the iris (figure 51 b)), the angle of view is smaller, and a lower portion of rays are obstructed by the rib, as the follow scheme explains, creating a deeper field-of-view, thus, give a more realistic image of the limit channel/rib. However, there should be a compromise between narrower or wider deep-of-field and the amount of light that passes through the iris.

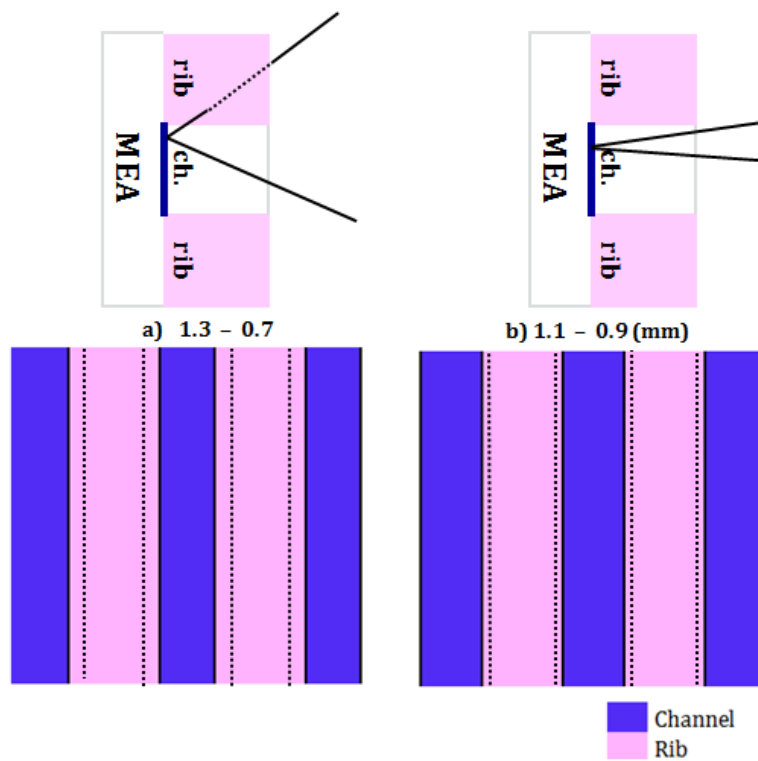


Figure 51: Scheme of the effect of iris aperture; a) iris open; b) iris narrow

4.2.4 Indexing the ribs

Each of the previous inspections into the channels and ribs was done by approximating the optical system to the most active area, given by the segmented cell. Segmented cell provides a general idea which area of the cell we are looking into, but it is not precise, in terms of what ribs and channels exactly we are focusing. A more accurate orientation technique would be of considerable improvement. As previously mentioned, the stainless steel has emissivity close to 0.77. A material with lower emissivity than anodized aluminum that could be fixed to the ribs would create an imaging contrast. According to this principle, aluminum foil with emissivity near to 0.04 was fixed along some ribs in different positions and sizes, signaling the ribs as a marker, see figure 51. Also, a non-transparent to infrared light tape was placed in the horizontal.

The resulting thermograms of this experiment can be observed in figure 52. As the figures show, it is possible to distinguish the markers in the ribs, due to the different emissivities of anodized and foil aluminum, despite a stronger contrast would be desirable. The two thermograms were both collected in the same conditions only differing in the color map.



Figure 51: Aluminum foil in the ribs

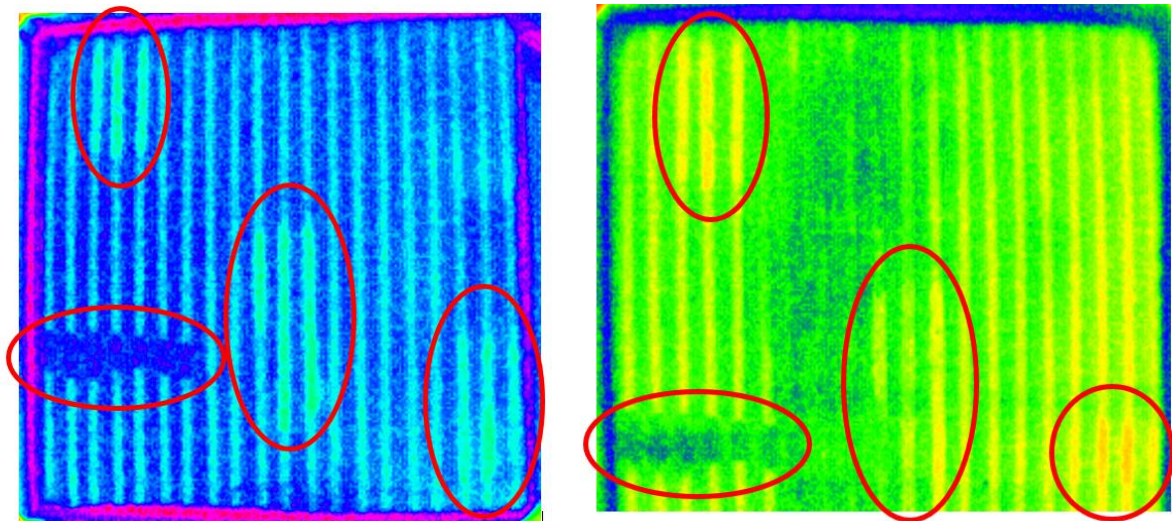


Figure 52: Two thermograms where is possible to distinguish the marked ribs

4.2.5 Applications and Limits

“Currently, the best method for optimizing fuel cell electrodes for water management is a tough and expensive trial-and-error process [43]”, says professor Jeff S. Allen, Microfluidics & Interfacial Transport Lab from Michigan University.

Following this, there is a wide range of future applications for infrared imaging applied to fuel cells, pushing the limits of the studies for several different studies.

As exemplified by **figure 42**, without magnification, it is possible to observe evolution of the waterfront along the channel tube with relative sharpness. The direct application of this IR imaging would be to develop studies to obtain water concentration distribution and the direct viewing liquid water paths through the small channels or where preferential water droplets

condensate in some regions of the cell, leading to studies in enhancing the operatory conditions to improve the fuel cell performance.

Some limitations related to camera pixel resolution still remain, and a camera with higher resolution would give us more detailed information about the shape of the droplet, velocity of formation of the droplets, size of the droplets, how water intrude the GDL, etc. Related to this, another limitation that was not solved was the permanent reflection of the camera in the window, and thus, some areas of the cell were not considered. The Germanium window that was previously mentioned would partially reduce the reflection because it's anti-reflective coating.

Related with magnified channels and ribs, another application also related with water management, is the study of local water accumulation, both formation or removal mechanisms. The channels are small enough that capillary forces are very important in some situations. The accurate study of multiphase flow and transport in the FC strongly depends on the accurate measurement of wettability properties of the GDL. In general, the conducted studies to measure GDL wettability are based on the external contact angle water-rib wall. By studies like those on pictures 47 and 49, further studies can be developed to understand what is the dominant mechanism for water removal for a given situation, either by the drag force or for capillary driven-flow. As described before, the properties of the camera (resolution, sensitivity) are limiting the applications and might be fine-tuned.

Another application that was explored is the temperature profile across the channels. However, there are some limitations related with heat diffusion, whoever it is from channels to the ribs, or the opposite. Different GDL with different thermal conductivities through plane were tested, but heat diffusion still occurs, despite it takes longer time. Still, we are limited by the fact we only know the thermal conductivities through plane, and the most important parameter to know would be the conductivity in the plane of the GDL.

As conclusion, the present system does not enable the study of temperature gradients across channels. A further work with very stable and very sensitive camera with sufficient resolution may achieve better results.

Finally, the possible resolution of the optical system - each IR optical system, regardless of equipment - is limited: the diffraction limit is given by half-the-wavelength. By the bottle neck effect of the series of optical components, the Si window limit is 4.5 μm , while Ge

would be around 5 μm , what become to be benefic, limiting the wavelength range, giving the image more resolution.

In this setup, with a Si window, the optical range of 7-9 μm , limits the theoretical resolution to 4.5 μm . The Ge window, that was mentioned before, would lead to even 5 μm , but the benefit of a broader spectral range and, thus, more light in the camera.

5 Conclusions

5.1 Accomplished objectives

The present work was a first development approach to study the potential of thermography with non-specialized camera applied to monitor fuel cell within the plates. In the first step, a new cell design was continuously developed to the point that the cell was able to run and produce a satisfactory current density, with controlled leakages. After this, the second part was to choose the reasonable optical materials and prepare an optic setup that allowed to observe through infrared wavelengths windows and lens, in order to look through the cathode plate. The first experiences, with no magnification, revealed that this technique is succeed in observe water emerging from the GDL, the paths where water preferentially accumulates and its evolution. The third part consisted in experiences to magnify the channels (1 mm) and ribs (1 mm), and thus, a combination of lenses was tested in order to accomplish it. A resolution of 44 pixels per channel (or 23 $\mu\text{m}/\text{pixel}$) was achieved and the two experiences done with this setup, with different operatory conditions, reveal two different mechanisms for water removal from the channels. This is a powerful result, showing the potential of thermography for this field. Further work should be explored but there is a confirmation that this technique has a range of applications previously described that can go from water management in the channels, solid-liquid particles interaction, heat management and its intercorrelations.

5.2 Limitations (Out look) and Future Work

Due to nature of this camera, which is limiting sensibility and resolution, applications in high magnification could not be pushed for studies at capillary scale. Nevertheless, since this work is a first step in using thermography to study phenomena within a fuel cell, much work must be done further.

The first step work is related with the fuel cell and equipment. Some leakages still occur in the cathode side: reducing the gas losses from the Silicon frame is a priority and despite the cell is operating, in order to achieve better current densities, this need to be improved. In relation to the window frame, it is suggested to use germanium windows instead of Silicon, due to the transmission curve of germanium which is more narrow for infrared wavelengths.

In order to continue this work to investigate water formation, both removal of formation and heat management, several works should be developed. The next step should be dedicating some work to optimize this system's optics. After pushing optics to its limits, I suggest the acquisition of a more sensitive camera with sufficient resolution to generally and locally study water management, and the way the water droplets intrude the channels.

A suggestion for a next experience is to use a membrane with gradients of catalyst to observe heat management within the cell.

5.3 Final appreciation

This work contributed to my personal growing in knowledge in the field of both fuel cells, infrared radiation and optical components, all them completely new to me. It was a hard challenge, nevertheless I finished it with the feeling of conquering, satisfaction and certain that chemical engineering, because it is all-embracing sciences gave me the confidence that I can learn any topic I decide to go deep. I can say now that one of the most important acquirements I got from this was the certainty that I can be whoever I want, as long as I fight everyday. Despite the hardness of quotidian, the only thing that matters is to keep my goals on my mind.

In terms of concretized work, the cell design was developed to a point that allows further investigations on the phenomena happening within the channels. This work, as a first approach to thermography applied to fuel cells, has several improvements that need to be done, despite it was proved that thermography has the potential to reveal some mechanisms that are still not totally explained. The scientific applications were previously described and this work started a technique that will contribute to the development of more effective MEA, as for example decreasing the loading of platinum in some areas of the MEA that reveal to be less active, decreasing the cost of the PEMFC, for later production and introduction in a viable market.

6 References

- [1] T. Wilberforce *et al.*, “Developments of electric cars and fuel cell hydrogen electric cars,” *Int. J. Hydrogen Energy*, vol. 42, no. 40, pp. 25695–25734, 2017.
- [2] B. Sørensen, “A renewable energy and hydrogen scenario for northern Europe,” *Int. J. Energy Res.*, vol. 32, no. 5, pp. 471–500, 2008.
- [3] P. W. Newton, “Innovation for a Sustainable Low Carbon Built Environment,” *ScienceDirect*, pp. 16–32, 2016.
- [4] International Energy Agency (IEA), International Energy Agency, and International Energy Agency (IEA), *World Energy Outlook 2014*. 2014.
- [5] I. Dincer, “Technical, environmental and exergetic aspects of hydrogen energy systems,” *Int. J. Hydrogen Energy*, vol. 27, no. 3, pp. 265–285, 2002.
- [6] H. Y. Kwak, H. S. Lee, J. Y. Jung, J. S. Jeon, and D. R. Park, “Exergetic and thermoeconomic analysis of a 200-kW phosphoric acid fuel cell plant,” *Fuel*, vol. 83, no. 14–15 SPEC. ISS., pp. 2087–2094, 2004.
- [7] M. L. S. Carnevali, “Modelling and Control of PEM Fuel Cells,” 2017.
- [8] S. Skoda, E. Robalinho, A. L. R. Paulino, E. F. Cunha, and M. Linardi, “Modeling of Liquid Water Distribution at Cathode Gas Flow Channels in Proton Exchange Membrane Fuel Cell-PEMFC,” vol. 617, no. 2008, p. 2008, 2010.
- [9] “DLR at a glance,” 2018. [Online]. Available: https://www.dlr.de/dlr/en/desktopdefault.aspx/tabid-10443/637_read-251/#/gallery/8570. [Accessed: 05-Nov-2018].
- [10] F. T. Bacon and H. K. Ihrig, “Applications of Fuel Cell Technology :,” pp. 39–43, 2018.
- [11] I. Pilatowsky, R. J. Romero, C. A. Isaza, S. A. Gamboa, P. J. Sebastian, and W. Rivera, “Thermodynamics of Fuel Cells,” pp. 25–36, 2011.
- [12] T. Maiyalagan and S. Pasupathi, *Components for PEM Fuel Cells: An Overview*, vol. 657, no. May 2014. 2010.
- [13] V. Mehta and J. S. Cooper, “Review and analysis of PEM fuel cell design and manufacturing,” *J. Power Sources*, vol. 114, no. 1, pp. 32–53, 2003.
- [14] D. G. Sanchez and P. L. Garcia-Ybarra, “PEMFC operation failure under severe dehydration,” *Int. J. Hydrogen Energy*, vol. 37, no. 8, pp. 7279–7288, 2012.
- [15] S. Basu, *Recent Trends in Fuel Cell Science and Technology*, vol. 39, no. 5. New Deli: Springer, 2007.
- [16] V. Rao, N. Kluy, W. Ju, and U. Stimming, “H,” in *Handbook of Membrane Separations: Chemical, Pharmaceutical, Food and Biotechnological Applications*, no. April, 2015, pp. 568–614.
- [17] “Nafion store,” 2018. [Online]. Available: http://www.nafionstore.com/store/pg/14-FAQ_US.aspx. [Accessed: 05-Nov-2018].
- [18] O. T. Holton and J. W. Stevenson, “The Role of Platinum in Proton Exchange Membrane Fuel Cells Evaluation of platinum’s unique properties for use in both the anode and cathode of a proton exchange membrane fuel cell,” *Platin. Met. Rev.*, vol. 57, no. 4, pp. 259–271, 2013.
- [19] B. Koraisly, J. Meyers, and K. Wood, “Manufacturing of membrane electrode assemblies for fuel cells,” *Trans. Int. Conf. Endod.*, pp. 1–13, 2009.
- [20] S. Litster and G. McLean, “PEM fuel cell electrodes,” *J. Power Sources*, vol. 130, no. 1–2, pp.

- 61–76, 2004.
- [21] N. Indayaningsih, Y. Irmawati, and F. Destyorini, “Performance of gas diffusion layer derived from carbon powder of coconut coir for PEMFC application,” *ARPN J. Eng. Appl. Sci.*, vol. 11, no. 6, pp. 4040–4044, 2016.
- [22] L. Carlos and P. Martínez, “Polymer Electrolyte Membrane Fuel Cells : Aging and Dynamic behaviour,” University of Porto, 2013.
- [23] T. Bewer, T. Beckmann, H. Dohle, J. Mergel, and D. Stolten, “Novel method for investigation of two-phase flow in liquid feed direct methanol fuel cells using an aqueous H₂O₂ solution,” *J. Power Sources*, vol. 125, no. 1, pp. 1–9, 2004.
- [24] Dr. Colleen Spiegel, “Education, Research and Fun since 1999,” 2017. [Online]. Available: <http://www.fuelcellstore.com/blog-section/fuel-cell-characterization>. [Accessed: 05-Nov-2018].
- [25] P. K. Bhattacharya, “Water flooding in the proton exchange membrane fuel cell,” *Directions*, vol. 15, no. 1, 2015.
- [26] S. A. Freunberger, M. Reum, A. Wokaun, and F. N. Büchi, “Measuring the Current Distribution with Submillimeter Resolution in PEFCs,” *J. Electrochem. Soc.*, vol. 156, no. 10, p. B1225, 2009.
- [27] I. Alaefour, “Current and Temperature Distributions in Proton Exchange Membrane Fuel Cell by,” University of Waterloo, 2012.
- [28] S. J. C. Cleghorn, C. R. Derouin, M. S. Wilson, and S. Gottesfeld, “A Printed Circuit Board approach to measuring current distribution in a fuel cell,” *J. Appl. Electrochem.*, vol. 28, no. 7, pp. 663–672, 1998.
- [29] M. Wilkinson *et al.*, “In Situ Experimental Technique for Measurement of Temperature and Current Distribution in Proton Exchange Membrane Fuel Cells,” *Electrochem. Solid-State Lett.*, vol. 9, no. 11, p. A507, 2006.
- [30] M. Wang, H. Guo, and C. Ma, “Temperature distribution on the MEA surface of a PEMFC with serpentine channel flow bed,” *J. Power Sources*, vol. 157, no. 1, pp. 181–187, 2006.
- [31] A. Collier, H. Wang, X. Zi Yuan, J. Zhang, and D. P. Wilkinson, “Degradation of polymer electrolyte membranes,” *Int. J. Hydrogen Energy*, vol. 31, no. 13, pp. 1838–1854, 2006.
- [32] F. A. De Bruijn, V. A. T. Dam, and G. J. M. Janssen, “Review: Durability and degradation issues of PEM fuel cell components,” *Fuel Cells*, vol. 8, no. 1, pp. 3–22, 2008.
- [33] T. F. Cao, Y. T. Mu, J. Ding, H. Lin, Y. L. He, and W. Q. Tao, “Modeling the temperature distribution and performance of a PEM fuel cell with thermal contact resistance,” *Int. J. Heat Mass Transf.*, vol. 87, pp. 544–556, 2015.
- [34] F. P. Incropera, D. P. Dewitt, T. L. Bergman, and A. S. Lavine, *Fundamentals of Heat and Mass Transfer*, Sixth Edit. John Wiley & Sons, 2006.
- [35] J. Tyson, “How Night Vision Works.” [Online]. Available: <https://electronics.howstuffworks.com/gadgets/high-tech-gadgets/nightvision2.htm>. [Accessed: 22-Dec-2018].
- [36] B. Griffith, D. Turler, and H. Goudey, “Infrared Thermographic Systems,” *The Encyclopedia of Imaging Science and Technology*. 2001.
- [37] A. Akula, R. Ghosh, and H. K. Sardana, “Thermal Imaging And Its Application In Defence Systems,” vol. 335, pp. 333–335, 2011.
- [38] R. Lin, H. Sander, E. Gülzow, and A. K. Friedrich, “Fuel Cells to Detect Malfunctions,”

- Electrochem. Soc.*, vol. 26, no. 1, pp. 229–236, 2010.
- [39] “Powerful thermal imaging cameras.” [Online]. Available: <https://www.thermal.com/compact-series.html>. [Accessed: 22-Jan-2019].
- [40] R. T. S. and M. W. D. Matthew J. Parry-Hill, “Image Formation with Converging Lenses.” [Online]. Available: <https://micro.magnet.fsu.edu/primer/java/lenses/converginglenses/index.html>. [Accessed: 12-Jan-2019].
- [41] Rob Dunsford, “Understanding Aperture: Take Control Of Depth Of Field For Professional Results.” [Online]. Available: <https://photographypro.com/aperture/>. [Accessed: 14-Jan-2019].
- [42] “ThorLabs: Optical coatings.” [Online]. Available: https://www.thorlabs.com/newgrouppage9.cfm?objectgroup_id=5840. [Accessed: 12-Jan-2019].
- [43] Jeffrey Allan, “Interfacial Phenomena: Where the Action Is,” 2010. [Online]. Available: <https://blogs.mtu.edu/mechanical/2010/07/26/interfacial-phenomena-where-the-action-is/>. [Accessed: 10-Feb-2019].

7 Appendix

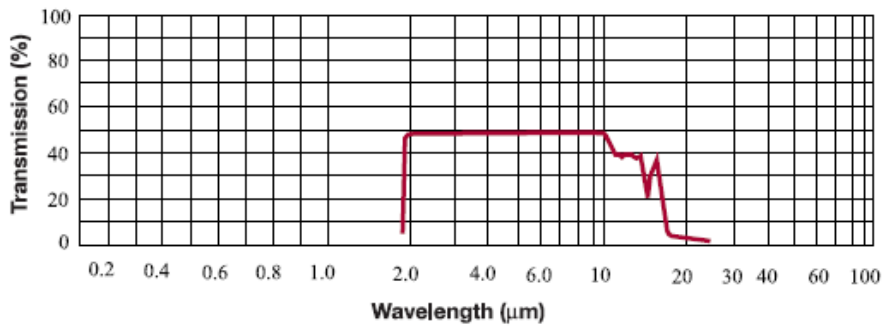


Figure 23: Germanium Transmission Curve

Table 5: Properties of Ge crystal

Properties of Germanium Crystal	
Transmission range (μm)	1.8 - 14.0
Refractive index @ 11 μm	4.0026
Reflection loss @ 11 μm (%)	53
Density (g.cm-3)	5.33
Thermal conductivity @ 293 K (W.m-1.K-1)	58.61
Coef. of Thermal expansion @ 298 K (°C-1)	6.1×10^{-6}
Solubility in water	insoluble
Molecular Weight	72.59
Structure	Cubic diamond

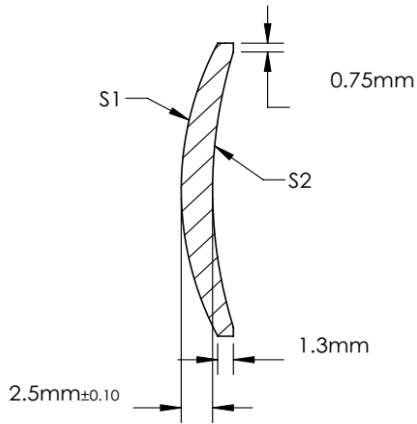


Figure 24: Germanium CAD meniscus lens, side view

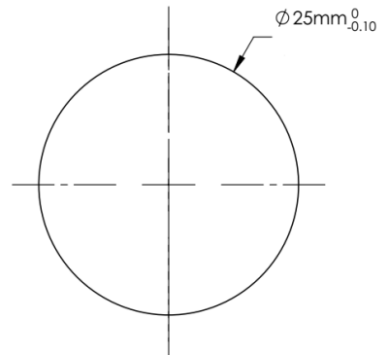


Figure 25: Germanium CAD meniscus lens, front view

	S1	S2
Shape	Convex	Concave
Radius	28.32	42.46
Clear aperture	$\geq \text{Ø } 22.50$	$\geq \text{Ø } 22.50$

Figure 26: Germanium meniscus lens features

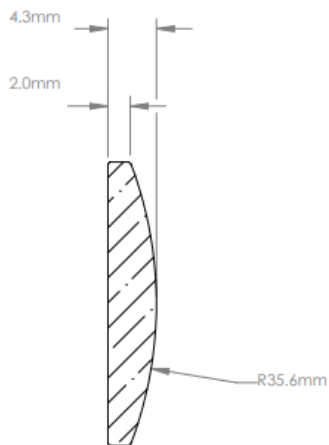


Figure 27: ZnSe CAD side view

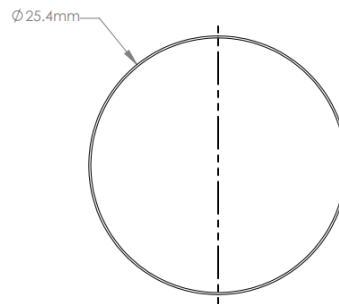


Figure 28: ZnSe CAD front view

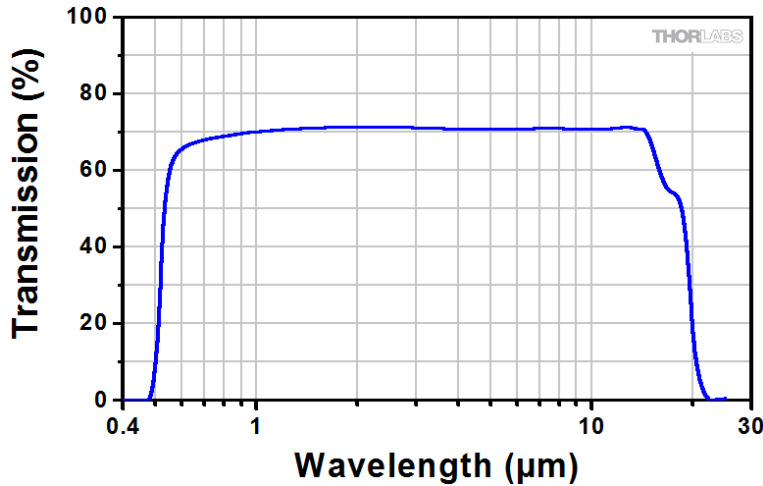


Figure 29: Zinc-Selenide Transmission Curve

Table 6: Properties of Zinc-Selenide

Properties of Zinc-Selenide	
Transmission range (μm)	0.6 - 21
Refractive index @ 10.6 μm	2.4028
Reflection loss @ 10.6 μm (%)	29.1
Density (g.cm^{-3})	5.27
Thermal conductivity @ 298 K ($\text{W.m}^{-1}\text{.K}^{-1}$)	18
Coef. of Thermal expansion @ 273 K ($^{\circ}\text{C}^{-1}$)	7.1×10^{-6}
Solubility in water ($\text{g}/100 \text{ g water}$)	0.001
Molecular Weight	144.33
Structure	FCC Cubic

Table 7: Properties of Silicon

Properties of Silicon	
Transmission range (μm)	1.2-10, 50-100
Refractive index @ 5 μm	3.426
Density @ 293 K (g.cm^{-3})	2.329
Thermal conductivity @ 300 K ($\text{W.m}^{-1}\text{.K}^{-1}$)	159
Coef. of Thermal expansion @ 273 K ($^{\circ}\text{C}^{-1}$)	2.55×10^{-6}
Solubility in water	insoluble
Molecular Weight	28.09
Structure	FCC Cubic

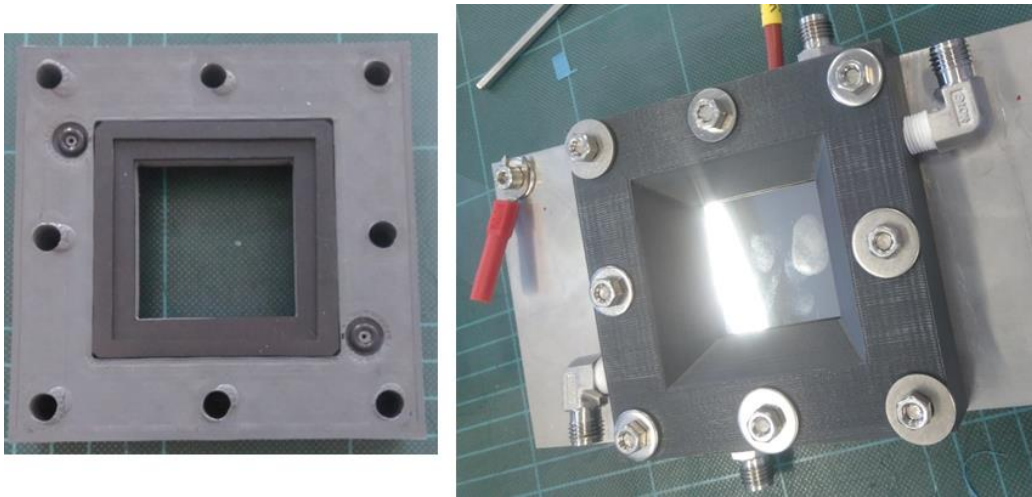


Figure 32: PLA Polymer plate

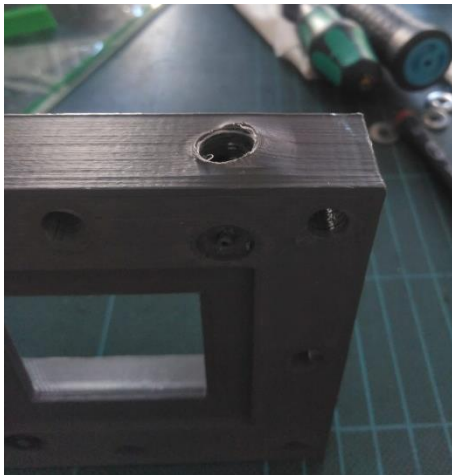


Figure 33: Deformation in the cathode plate inlet

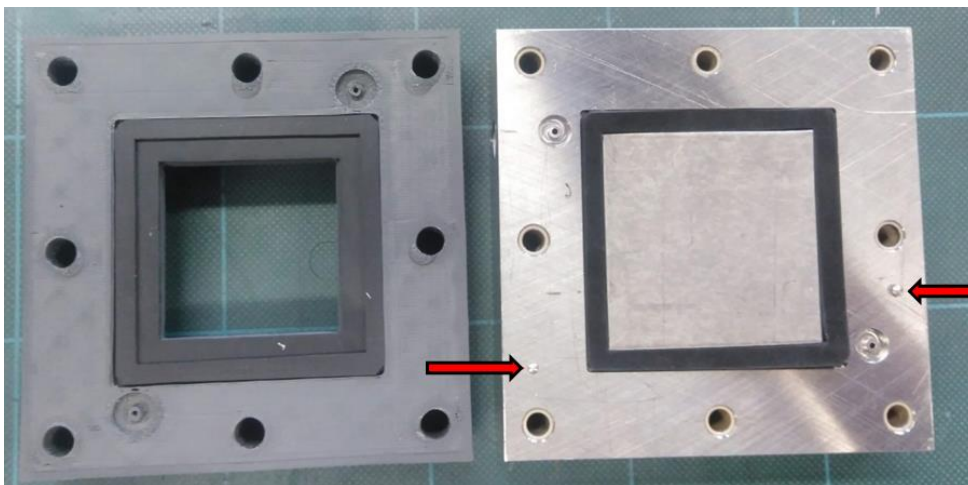


Figure 34: Substitution of the polymer plate

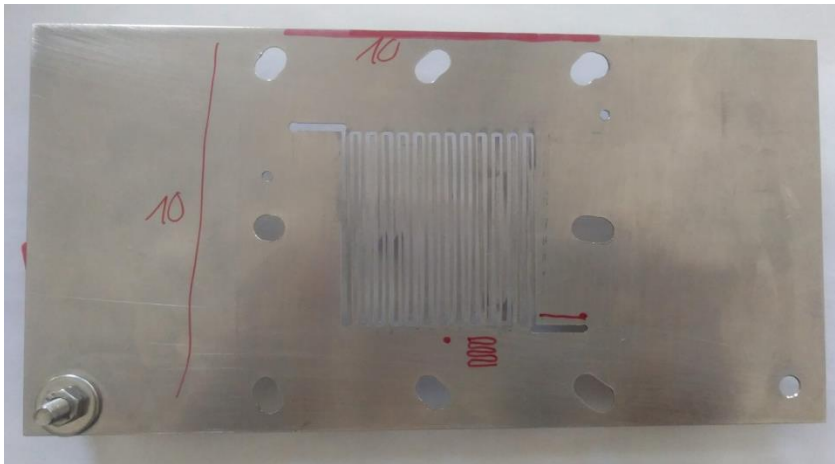


Figure 35: First version of the flowfield

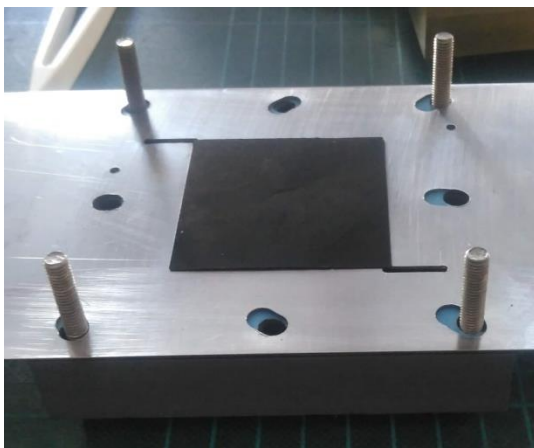


Figure 36: Flowfield and GDL



Figure 37: Close view from inlet and flowfield path

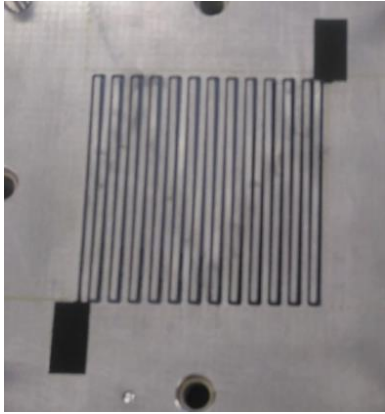


Figure 38: Flowfield pathways with GDL

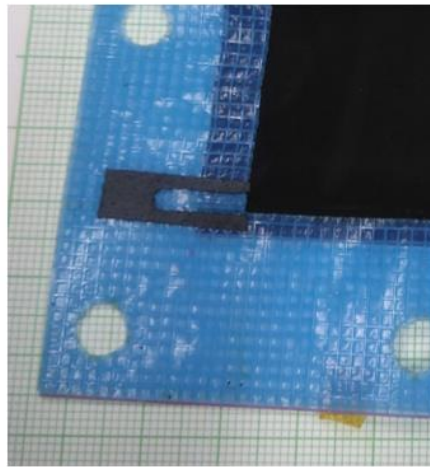
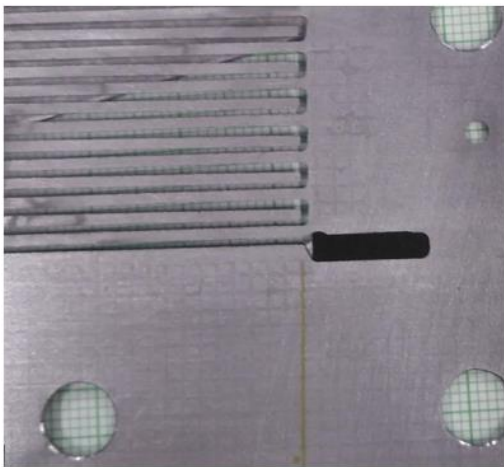


Figure 39: GDL obstructing the flowfield pathway



Figure 40: Silicon cut off-axis testing

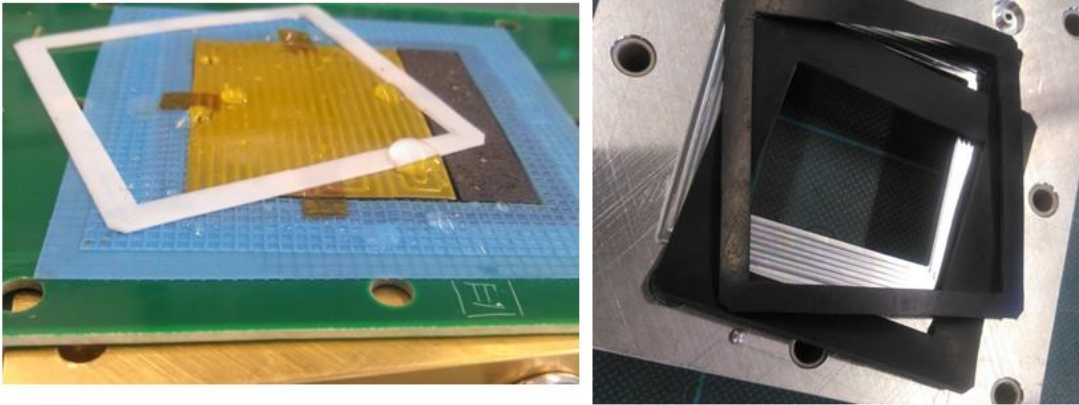


Figure 41: Set of Viton sheets tested to control the leaks in the frame

Table 10: Types of aberrations and respective correction

Aberration	Character	Correction
Spherical aberration	Monochromatic, on- and off-axis, image blur	Bending, high index, aspherics, gradient index, doublet
Coma	Monochromatic, off-axis only, blur	Bending, spaced doublet with central stop
Oblique astigmatism	Monochromatic, off-axis blur	Spaced doublet with stop
Curvature of field	Monochromatic, off-axis	Spaced doublet
Distortion	Monochromatic, off-axis	Spaced doublet with stop
Chromatic aberration	Heterochromatic, on- and off-axis, blur	Contact doublet, spaced doublet

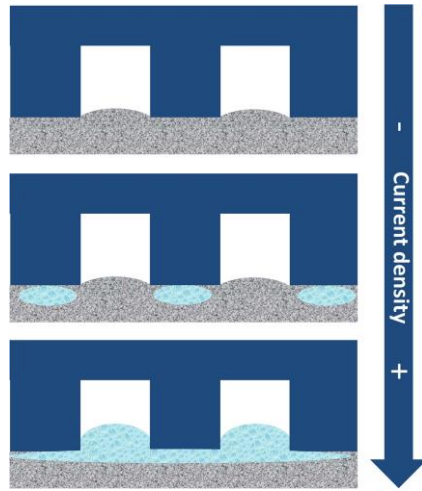


Figure 48: Water accumulation process under-ribs

